

THE *SPITZER*-IRAC POINT-SOURCE CATALOG OF THE VELA-D CLOUD

F. STRAFELLA¹, D. ELIA^{1,2}, L. CAMPEGGIO¹, T. GIANNINI³, D. LORENZETTI³, M. MARENGO⁴, H. A. SMITH⁵, G. FAZIO⁵,
M. DE LUCA^{3,6}, AND F. MASSI⁷

¹ Dipartimento di Fisica, Università del Salento, CP 193, 73100 Lecce, Italy; francesco.strafella, loretta.campeggio@le.infn.it

² Universidade de Lisboa, Faculdade de Ciências, Centro de Astronomia e Astrofísica, Observatório Astronómico de Lisboa, Tapada da Ajuda 1349-018, Lisboa, Portugal; eliad@oal.ul.pt

³ INAF-Osservatorio Astronomico di Roma, via Frascati 33, I-00040 Monte Porzio, Italy; giannini@oa-roma.inaf.it, dloren@oa-roma.inaf.it

⁴ Department of Physics and Astronomy, Iowa State University, Ames, IA 50011, USA

⁵ Harvard-Smithsonian Center for Astrophysics, Cambridge, MA 02138, USA; mmarengo@cfa.harvard.edu, hsmith@cfa.harvard.edu

⁶ LERMA-LRA, UMR 8112, CNRS, Observatoire de Paris and Ecole Normale Supérieure, 24 Rue Lhomond, 75231 Paris, France; massimo.de.luca@ira.ens.fr

⁷ INAF-Osservatorio Astrofisico di Arcetri, Largo E. Fermi 5, 50125 Firenze, Italy; fmassi@arcetri.astro.it

Received 2009 November 12; accepted 2010 May 28; published 2010 July 16

ABSTRACT

This paper presents the observations of Cloud D in the Vela Molecular Ridge, obtained with the Infrared Array Camera (IRAC) camera on board the *Spitzer Space Telescope* at the wavelengths $\lambda = 3.6, 4.5, 5.8,$ and $8.0 \mu\text{m}$. A photometric catalog of point sources, covering a field of approximately 1.2 deg^2 , has been extracted and complemented with additional available observational data in the millimeter region. Previous observations of the same region, obtained with the *Spitzer* MIPS camera in the photometric bands at $24 \mu\text{m}$ and $70 \mu\text{m}$, have also been reconsidered to allow an estimate of the spectral slope of the sources in a wider spectral range. A total of 170,299 point sources, detected at the 5σ sensitivity level in at least one of the IRAC bands, have been reported in the catalog. There were 8796 sources for which good quality photometry was obtained in all four IRAC bands. For this sample, a preliminary characterization of the young stellar population based on the determination of spectral slope is discussed; combining this with diagnostics in the color–magnitude and color–color diagrams, the relative population of young stellar objects (YSOs) in different evolutionary classes has been estimated and a total of 637 candidate YSOs have been selected. The main differences in their relative abundances have been highlighted and a brief account for their spatial distribution is given. The star formation rate has also been estimated and compared with the values derived for other star-forming regions. Finally, an analysis of the spatial distribution of the sources by means of the two-point correlation function shows that the younger population, constituted by the Class I and flat-spectrum sources, is significantly more clustered than the Class II and III sources.

Key words: infrared: stars – ISM: clouds – ISM: individual objects (Vela Molecular Ridge) – stars: formation – stars: pre-main sequence – surveys

Online-only material: color figures, machine-readable tables

1. INTRODUCTION

The Vela Molecular Ridge (hereinafter VMR) is a cloud complex constituted by four giant molecular clouds (Murphy & May 1991), hosting large regions of active star formation (hereinafter SF), in which low- and intermediate-mass stars are forming (Liseau et al. 1992). Its position on the Galactic plane ($272^\circ \gtrsim \ell \gtrsim 260^\circ$; $3^\circ \gtrsim b \gtrsim -3^\circ$) makes this complex a unique laboratory for studying the SF phenomenon when the environmental conditions are those typical of the Galactic disk. This is an important point to consider in extrapolating global SF parameters to the Galactic scale. Indeed, the most commonly studied SF regions are projected outside the Galactic plane, in part because of the observational need to minimize the source confusion. The drawback is that the global quantities derived for these regions could not be fully representative of the bulk of the SF in the Galaxy.

Our study is focused on a particular subregion of the Vela cloud complex, the so-called D cloud (Murphy & May 1991; hereinafter VMR-D), which has already been the subject of previous papers by our group. Former studies have shown a rich phenomenology associated with this cloud, involving outflows (Wouterloot & Brand 1999; Elia et al. 2007), jets (Lorenzetti et al. 2002; Giannini et al. 2005), and evidence of clustered and isolated SF (Massi et al. 2000, 2003). After

the CO emission survey of the whole VMR carried out by Yamaguchi et al. (1999), two maps of a $\approx 1 \text{ deg}^2$ region of VMR-D were obtained with higher resolution by Elia et al. (2007; $^{12}\text{CO}(1-0)$ and $^{13}\text{CO}(2-1)$ emission lines) and Massi et al. (2007; millimeter dust continuum), aimed at studying the cloud morphology and properties as well as their relationships with the SF process active in this region (see also De Luca et al. 2007). This molecular cloud has been recently observed with both Multiband Imaging Photometer for *Spitzer* (MIPS) and Infrared Array Camera (IRAC) on board the *Spitzer Space Telescope* and the MIPS aperture photometry has already been the subject of a previous work (Giannini et al. 2007).

In this paper, we present the analysis of the *Spitzer*-IRAC mosaics of the VMR-D cloud, covering a region that mostly overlaps the field observed at longer wavelengths by MIPS and also corresponding to the sky regions already mapped in the millimeter spectral range and discussed in the previous papers. These new IRAC observations allowed us to compile a four-band photometric catalog of point sources that, complemented by the information previously obtained at longer wavelengths, constitutes a unique data bank for studying the young stellar objects (YSOs) in this cloud. With this as our goal, we have also revisited the photometric analysis of the MIPS $24 \mu\text{m}$ and $70 \mu\text{m}$ mosaics to obtain more accurate point-spread function (PSF) photometry. The inclusion of the longer wavelength photometry

is motivated by our aim to determine, as accurately as possible, the spectral slopes of the sources, infer their evolutionary stages, and obtain a reliable statistical description of the YSO population.

A particularly valuable characteristic of our IRAC observations is that the data were collected by splitting the total integration time into two observing epochs 4.5 months apart, thereby enabling a first exploration of source variability in VMR-D. Indeed we found a number of sources that clearly showed brightness variations; they constitute a significant subsample deserving special attention, and are discussed in a separate paper (Giannini et al. 2009).

This paper is organized as follows: after a brief description of the observations in Section 2, we give an account of the procedure followed for source extraction and photometry for both IRAC and MIPS data in Section 3. In the same section, we also discuss the source selection criteria as well as the completeness and reliability. The final VMR-D point-source catalog is presented in Section 4. In Section 5, we focus our attention on a subsample of 8796 sources (out of a total of 170,299) that have been detected in all the four IRAC bands and for which good quality photometry was obtained. In the following we shall refer to this subsample as the “working sample.” By means of color–color and color–magnitude diagrams, we select the candidate YSOs obtaining a census of the YSO content of the VMR-D region. In this same section, a brief account of the clustering properties is done. Our conclusions are summarized in Section 6.

2. OBSERVATIONS

The observations were carried out with the IRAC (Fazio et al. 2004) on board the *Spitzer Space Telescope* (Werner et al. 2004). The data were obtained as part of the *Spitzer/IRAC Cycle 3 GTO* (PID 30335, PI: G. Fazio). The Galactic region observed was delimited in longitude by $264^{\circ}29' \gtrsim \ell \gtrsim 263^{\circ}00'$ and in latitude by $0^{\circ}42' \gtrsim b \gtrsim -0^{\circ}50'$, covering about 1.2 deg^2 . This field corresponds to a significant portion of the VMR-D cloud that has been mapped in four spectral bands, corresponding to the four IRAC camera detectors observing at the wavelengths $\lambda = 3.6, 4.5, 5.8, \text{ and } 8.0 \mu\text{m}$, respectively. The effective integration time per pixel, $t_{\text{exp}} = 20.8 \text{ s}$ in each band, has been accumulated by splitting the observations in two epochs separated by 4.5 months, a choice mainly dictated by the desire to monitor the observed region for possible variability of the sources. The same splitting of the observation time into two epochs has also been beneficial for a better cleaning of artifacts from the final mosaics.

The IRAC data were obtained by mapping the whole region, in each epoch, with 12×14 tiles, each observed in two dither positions. The observation was performed in IRAC 12 s High Dynamic Range (HDR) mode, consisting of two consecutive integrations of 0.4 and 10.4 s exposure times. The HDR mode was chosen to limit the saturation effects around the bright regions, a problem which is clearly present in the long exposure images in the neighborhood of the brightest sources. The data were reduced using the IRACproc package (Schuster et al. 2006) to combine the individual tiles into a flux calibrated mosaic on a pixel grid of $0''.8627 \text{ pixel}^{-1}$. IRACproc is a wrapper for the Spitzer Science Center mosaic software MOPEX and provides enhanced outlier (cosmic rays) rejection.

Thus for each spectral band, we obtained a total of four mosaics, one long and the other short exposure for each of the two epochs. The mosaics of each epoch were subsequently co-added to obtain two final mosaics in each IRAC band, one

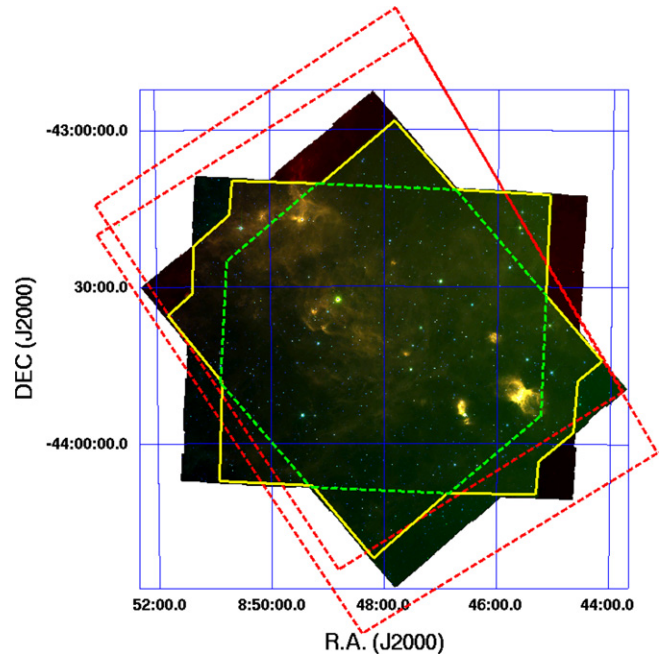


Figure 1. Three-color image of the observed field, obtained by the superposition of the mosaics acquired in different bands. The color coding is blue, green, and red for $\lambda = 3.6, 5.8, \text{ and } 8.0 \mu\text{m}$, respectively. A yellow contour line delimits the region imaged in all four IRAC bands. The geometry of the scans, obtained in two different epochs, is such that only the central part of the field (dashed green line) is observed twice, while more external regions are covered only once. The more external red dashed lines delimit the fields observed with MIPS at $24 \mu\text{m}$ (upper) and $70 \mu\text{m}$ (lower), respectively.

(A color version of this figure is available in the online journal.)

with the long ($t_{\text{exp}} = 20.8 \text{ s}$) and the other with the short ($t_{\text{exp}} = 0.8 \text{ s}$) total exposure time. However, due to the different orientation constraints in the two observing epochs, and due to the fact that the four IRAC cameras do not see exactly the same fields simultaneously, the images obtained in the two epochs do not fully overlap. As a consequence, in the co-added mosaic the region corresponding to the full exposure time is limited by the spatial overlap of the mosaics obtained in the two observing epochs. The final mosaics therefore include a central region, observed for the total integration time $t_{\text{exp}} = 20.8 \text{ s}$, as well as adjacent surrounding regions corresponding to the non-overlapping fields that have been imaged only in one of the two epochs for a total exposure time $t_{\text{exp}} = 10.4 \text{ s}$. The geometry of the mapping and the different parts covered are shown in Figure 1. In the following, we shall consider the whole region observed in the four bands, delimited in Figure 1 by the yellow contour, to produce the corresponding point-source catalog, recalling that the area that has been imaged in both epochs, included in the green dashed contour, is clearly the region observed with a slightly higher signal-to-noise ratio (S/N). In producing this catalog, we also take advantage of our previous observations of the VMR-D region to assess if a source falls on the mapped CO-emitting cloud or not. This evaluation is important and interesting in this context because we do not have adequate off-source observations of control fields, and the archival ^{12}CO observations allow us to evaluate, at least to a first approximation, the possible contamination of the ON-cloud YSO population by OFF-cloud background/foreground objects. Operatively, we shall consider a source as projected on the molecular cloud, i.e., ON-cloud, if it is contained within the ^{12}CO contour line corresponding to the 5 K km s^{-1} level in the integrated intensity map of Elia et al. (2007) which is shown

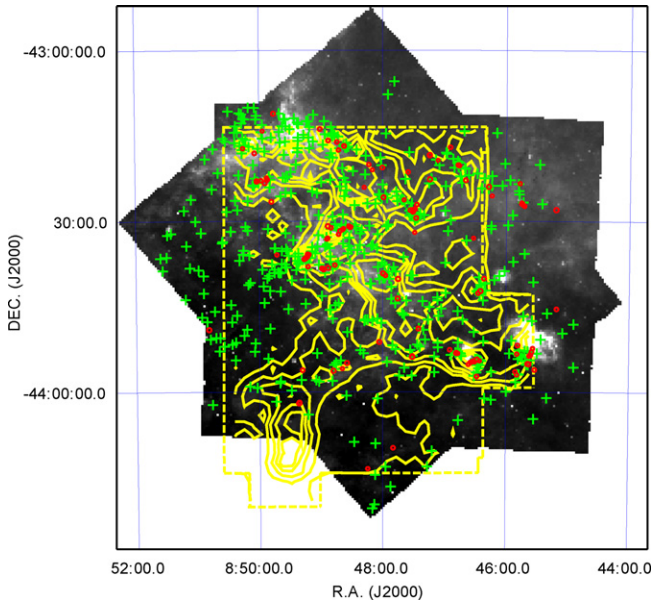


Figure 2. ^{12}CO contours from Elia et al. (2007) are reported (yellow line) superposed to the IRAC $8.0\ \mu\text{m}$ mosaic, starting at $5\ \text{K km s}^{-1}$ in steps of $15\ \text{K}$ (km s^{-1}). The yellow dashed line delimits the region observed in ^{12}CO . The spatial distribution of the Class I/flat (red circles) and the Class II/III (green crosses) is also shown. The reported sources are those recognized as bona fide YSOs by using the selection criteria of Harvey et al. (2007) and the exclusion criteria of Gutermuth et al. (2009) discussed in Section 5.1.1 and illustrated in Figures 8–10.

(A color version of this figure is available in the online journal.)

superimposed on the IRAC $8\ \mu\text{m}$ mosaic in Figure 2. Clearly, this is only a necessary condition for a source to be considered for additional constraints aimed at discriminating bona fide ON-cloud YSOs from galactic/extragalactic contaminants.

3. SOURCE EXTRACTION AND PHOTOMETRY

To obtain the photometric information on the point sources detected in our mosaics, we adopted the DAOPHOT (Stetson 1987) photometric package. This offers a consolidated suite of algorithms aimed at detecting all the possible point-like objects whose signals are larger than a predefined threshold. The photometry was derived on our final (two epochs combined) mosaics. Single epoch photometry was however also measured for some sources, in order to assess the reliability of our final catalog. In this section, we shall describe the methods used for source detection and photometry, as well as the selection criteria adopted for compiling the VMR-D point-source catalog. Completeness and reliability is also discussed and finally the MIPS mosaics are reconsidered in order to obtain a PSF photometry to be used as a complement to the IRAC catalog.

3.1. Source Detection

Due to the large spatial extent of our mosaics and to the presence of extended bright nebulosity, distinct, local background intensity gradients are invariably present, so that it is not advisable to simply scan the original image with a given sensitivity threshold. The output of the detection algorithms in this case would be affected by a spatially variable sensitivity, depending on the different levels of the local background, a problem that is made even worse when strong gradients are present.

To ameliorate this difficulty, we first evaluated the PSF of our mosaics by using relatively isolated, bright, unsaturated stars, and then performed PSF point-source subtractions to remove,

to first order, the point-like objects. In this way, we obtained images practically devoid of strong point sources, even if some residuals are clearly present. We used these images to estimate the background level across the whole field, a step that was done in each observed band by evaluating the sky value around each pixel in a square box of 51 pixels in size. This was done by using the DAOPHOT-SKY procedure that estimates the modal value after clipping the outliers. Note that the relatively large size adopted for the scanning box is justified by the need to include a sufficient number of sky pixels even in crowded images, as is the case particularly for the first two IRAC bands centered at $\lambda = 3.6\ \mu\text{m}$ and $\lambda = 4.5\ \mu\text{m}$, respectively.

Once the background in each band was obtained and subsequently subtracted from the original mosaics, we were left with four background-subtracted images in which the large-scale gradients were strongly smoothed while the small-scale noise was preserved. At this point, the compatibility of the noise with Poissonian statistics is recovered by adding the original mean sky value back onto the background-subtracted images that were then used in the photometry extractions.

Source detection was then performed by scanning these final images with a star finding procedure which is based on a convolution with a wavelet-like filter whose spatial extent has been tuned to match the size of the point-like objects in the image. The signal produced by this convolution is then analyzed at different detection thresholds that, in our case, were taken at 5σ and 10σ , respectively.

3.2. Photometry

Once we had the list of detections from the star finding algorithm, we used aperture photometry to obtain a first evaluation of the source magnitudes. Although this is a relatively inaccurate method when crowding or background gradients are present in the image, it is nevertheless useful for a first estimate of source brightness, an information that was used later as a starting point for more accurate photometry.

The final magnitude values were indeed obtained by means of an iterative PSF-fitting procedure that, in the implementation adopted by DAOPHOT, is based on an estimate of the instrumental PSF obtained from stellar images appearing relatively isolated in the frame. However, because the PSF is undersampled by the IRAC cameras, the corresponding point response function (PRF) that we obtain from our mosaics cannot be completely accurately determined; this produces a corresponding uncertainty in the subsequent fit to the stellar images. In spite of this difficulty, the photometry resulting from this method can be considered more accurate than the aperture photometry because the differences in fitting the PRF to the stellar images remain approximately balanced between positive and negative residuals. In this way, the total flux is substantially preserved, even in presence of residuals, although at the cost of an increased uncertainty in the fitting parameters (see also Section 3.4 on reliability). The PRF we used is actually a combination of an analytic function (in our case a Lorentzian showed better results in minimizing the residuals) and a look-up table whose aim is to compensate for systematic differences between the pure analytic function and the actual stellar images. An example of the residuals remaining after subtraction of the modeled sources from the IRAC mosaics is shown in Figure 3, which illustrates this point for the two IRAC mosaics obtained at $3.6\ \mu\text{m}$ (upper panels) and the $8.0\ \mu\text{m}$ (lower panels), respectively.

Note, however, that the knowledge of the PRF also allowed us to take into account, and then correct for, the contribution to

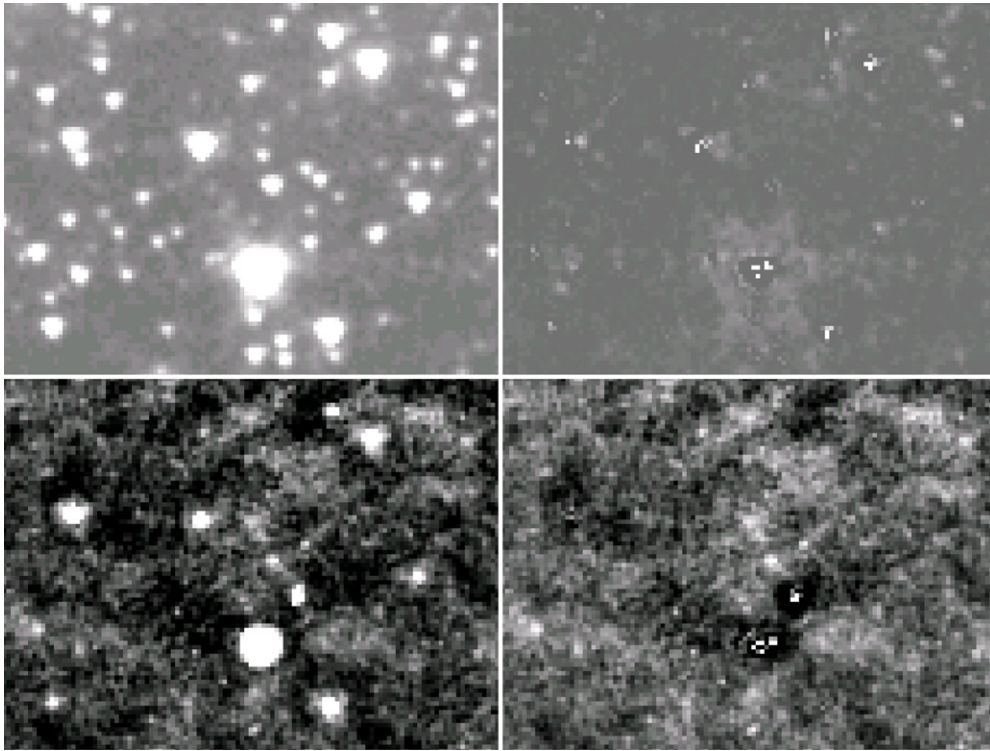


Figure 3. Portion of VMR-D cloud delimited by $\alpha = (08^{\text{h}}47^{\text{m}}45^{\text{s}})$ and $\delta = (-43^{\circ}57'54'')$ at the lower left corner, and by $\alpha = (08^{\text{h}}47^{\text{m}}36^{\text{s}})$ and $\delta = (-43^{\circ}56'41'')$ in the upper right. The left panels show the mosaics obtained at $3.6 \mu\text{m}$ (upper) and $8.0 \mu\text{m}$ (lower), respectively. The right panels illustrate the residuals remaining after subtraction of the point sources that have been modeled with the PRF obtained by using isolated unsaturated stars in the same mosaics.

the flux of a source from wings in the brightness distribution of its neighboring sources. This advantage is fully exploited in crowded regions because the photometric values are obtained only after convergence of an iterative procedure that fits simultaneously groups of nearby stars instead of single objects.

3.3. Point-source Selection

We selected the sources to be included in our catalog by applying to the photometric lists obtained from the long exposure mosaics a sequence of logical filters based on a reasonable use of the quality parameters associated with the photometric procedures.

3.3.1. Automatically Selected Sources

Our first choice was to consider as “good photometry sources” only those detected above the 5σ threshold of the background noise. To easily distinguish faint and bright sources in the catalog, we also flagged those detected above the 10σ threshold.

The DAOPHOT procedure for obtaining the point-source photometry, besides evaluating the brightness, also computes two additional quantities: *CHI* and *SHA*, related to the goodness of the fit and to the source sharpness, respectively. Here, *CHI* is evaluated as the ratio between the observed scatter in the fitting residuals and that expected on the basis of the pure image noise, and is a measure of the departure of the source image from the model PRF. The sharpness parameter *SHA*, instead, is computed as a difference between the square of the size, in pixels, of a given source and the same quantity computed for the fitting PRF so that it can be used, within certain limits, as an indicator of the source angular extent.

At first we constrained these two parameters to be $CHI < 3$ and $|SHA| < 0.7$ to represent bona fide point-like sources; we

subsequently applied a further criterion to the flux uncertainty to select only sources with a flux relative error $\delta F/F < 0.5$. As a third step, we also considered the number of iterations needed for the PRF fitting algorithm to converge on a given source: to avoid the worst cases, mainly corresponding to faint sources in crowded fields, we limited selections to those sources requiring fewer than eight iterations. Finally, because the PRF fitting procedure also implies a recentering of the source position, we filtered out all those sources in which the corresponding best-fit centroid was displaced from the original position as evaluated in the previous detection phase by more than $1''$.

3.3.2. Manually Dropped Sources

Despite all our efforts to select genuine point sources, the photometric lists still included many detections that, on visual inspection, are actually artifacts in the vicinity of the brightest sources.⁸ This problem affects in particular the mosaics at $\lambda = 3.6 \mu\text{m}$ and $\lambda = 4.5 \mu\text{m}$, and is related to the so-called *muxbleed* defect. These artifacts are recognized because they appear as a sequence of equally spaced pseudo-sources aligned along the same row containing the true bright source. Because their appearance is very much like that of a train of point sources, these pseudo-sources escaped all our other selection filters so that it was necessary to eliminate them by eye. In this way, more than 1000 false sources were discarded.

3.3.3. Additional Sources and Short Exposures

Besides these false sources, the previous selection criteria, applied to the long exposure photometry, discarded an additional, but relatively small, number of sources (~ 1000). These

⁸ See the IRAC Data Handbook, version 3.0, available at <http://ssc.spitzer.caltech.edu/irac/dh/>.

Table 1
Overview of the Limiting Magnitudes and Completeness

| Quantity | IRAC | | | | MIPS | |
|---------------------|----------------------|----------------------|----------------------|----------------------|----------------------|----------------------|
| | 3.6 | 4.5 | 5.8 | 8.0 | 24 | 70 |
| F_{lim}^a | 1.1×10^{-5} | 1.0×10^{-5} | 3.5×10^{-5} | 4.9×10^{-5} | 6.3×10^{-4} | 1.0×10^{-1} |
| m_{lim} | 18.5 | 18.1 | 16.3 | 15.3 | 10.1 | 2.2 |
| F_{comp}^a | 4.9×10^{-5} | 4.5×10^{-5} | 2.9×10^{-4} | 4.0×10^{-4} | 2.0×10^{-3} | 5.0×10^{-1} |
| m_{comp} | 16.9 | 16.5 | 14.0 | 13.0 | 8.9 | 1.0 |

Note. ^a All fluxes are given in Jy.

are mainly located in regions affected by crowding or saturation, the latter case occurring especially in the neighborhood of the brightest objects. To compensate for this, we also considered the short exposure mosaics, obtaining the corresponding photometry with the same procedure adopted for the long exposures. The short exposure photometry was used when, in assembling the catalog, the long exposure photometry of a given source was rejected due to one of the adopted selection criteria, as opposed to pixel replacement in the mosaic or a hard cutoff between the short and long frames. In these cases, we further checked to see if alternative, short exposure photometry existed that met all the catalog constraints. If it did, we included the source in the catalog; in this way we recovered a total of 276 sources.

We also re-examined an additional 77 rejected sources, most of which (68 cases) are associated with $24 \mu\text{m}$ MIPS sources that escaped IRAC detection because they are either so bright they suffered saturation effects or were embedded in a bright nebulosity. For most of these sources, we used the short exposure mosaics to obtain the photometry even though it is more uncertain. These objects were included in the catalog to produce a list as complete as possible, even though they have been flagged as “bad photometry” and are not considered further in the analysis of the YSO population. However, the reader can use these flux densities with their uncertainties, but at the same time should be aware that the corresponding quality flags do not satisfy all the constraints previously discussed for the automatic source selection.

In conclusion, we obtained four lists of sources, one for each IRAC band, that have been spatially delimited to include only objects lying in the sky region surveyed in all the four IRAC bands as delimited by the yellow contour line in Figure 1.

3.4. Sensitivity, Completeness, and Reliability

An upper limit to the completeness of our catalog is clearly set by the sensitivity detection threshold adopted in the detection phase that, we recall, was set to 5σ . This threshold corresponds to different limiting flux densities because the background level changes with the wavelength. We evaluated the limiting flux densities in each spectral band by calculating the average value of the pixel fluctuation in the background images obtained in the course of the photometric procedure. The same limiting flux densities are independently derived from the magnitude plots of Figure 4, showing the distribution of the catalog point sources as a function of their magnitude in the four IRAC bands. From these plots, it is apparent that the logarithm of the number of sources increases proportionally to the magnitude, until the linear behavior is lost and a fall in the number of sources is clearly seen. The vertical line drawn in each panel denotes the largest magnitude at which the catalog can be considered as complete, a value that is clearly lower than the limiting magnitude. These values are summarized in Table 1 along with their corresponding flux densities.

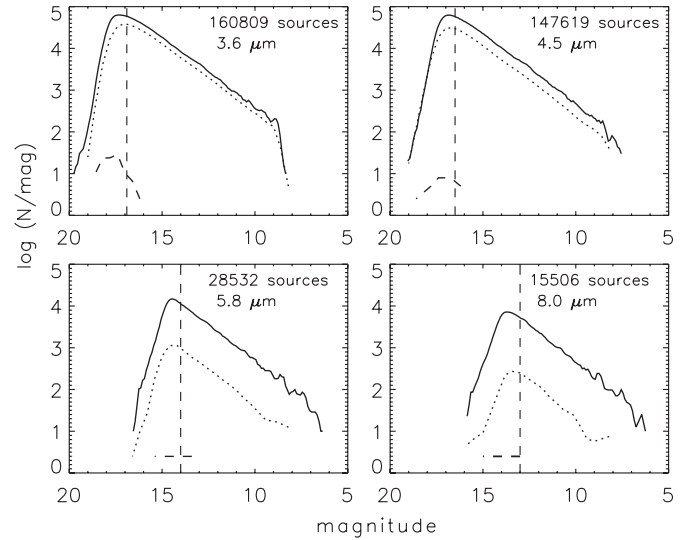


Figure 4. Distribution of the magnitudes in the VMR-D catalog. Each panel corresponds to an IRAC band, as indicated. The upper curve (continuous line) represents all the sources included in the catalog. The dotted line refers to sources observed in both observing epochs (i.e., falling within the green dashed line in Figure 1). Here, the sources included are either detected twice or once but with a detection in an adjacent band. The lower dashed curve corresponds to sources considered unreliable because they are detected only once, without any detection in adjacent bands. From these distributions, the catalog completeness and the reliability are estimated (see the text). The vertical dashed line is drawn to mark the completeness limit.

As far as the reliability is concerned, we can exploit the fact that the VMR-D field was observed twice, allowing a check on the source detections. The criterion we adopt for this evaluation is to consider as reliable detections in a given IRAC band two possible cases: (1) sources detected in both observing epochs and (2) sources detected only once but showing at least another detection in an adjacent band. On the other hand, we consider as less reliable detections case (3) when sources were detected only once in a given band and with no detection in the adjacent bands.

To ensure that the sources we consider in estimating the reliability were observed twice, we restricted this analysis to the area delimited by the overlap of the IRAC mosaics from both epochs (dashed green line in Figure 1). Applying to these sources the previous criteria, we obtain the distributions shown in Figure 4 as a dotted (reliable) and dashed (unreliable) line. From these plots, we estimate the reliability as a function of the magnitude by ratioing the number of sources satisfying criteria (1) and (2) with the totality of the catalog sources (1)+(2)+(3) in a given band and magnitude interval. In this way, we derive a reliability estimate that is always larger than 99% in the whole magnitude range.

All the sources observed in both epochs show flux densities that are compatible within their uncertainties; the very few

sources (around 0.2%) showing a significant photometric variability have been discussed in Giannini et al. (2009).

3.5. MIPS Photometry

As mentioned in Section 1, we also reconsidered the MIPS observations at $24\ \mu\text{m}$ and $70\ \mu\text{m}$ of the VMR-D region covering a slightly larger field of approximately $1.8\ \text{deg}^2$ (see Figure 1). These observations have already been presented by Giannini et al. (2007), who reported the aperture photometry for 849 and 61 sources in the $24\ \mu\text{m}$ and $70\ \mu\text{m}$ band, respectively.

However, because aperture photometry tends to be less accurate in the presence of large background gradients such as those present in the MIPS VMR-D mosaics, in Giannini et al. (2007) the MIPS sources considered were limited to those in regions where reliable aperture photometry was possible. Because PSF-fitting photometry is a more accurate tool, we re-analyzed the regions in the two MIPS mosaics of VMR-D to obtain a revised list of sources with the corresponding PSF photometry. Our aim was to obtain more accurate spectral energy distributions (SEDs) and then a more reliable determination of the spectral slopes characterizing the YSO population.

The analysis of the MIPS mosaics was done with the same procedures described for the IRAC images. First, we minimized the effects of the background variations by obtaining a rough subtraction of the point sources from the original image. After this first step eliminated most of the point-source signal, the mosaics were scanned with a square box of 21 pixels on a side to produce an estimated background image. This in turn was subtracted from the original mosaic producing a flattening of the large-scale gradients, thus allowing a subsequent point-source detection across the field with a much more uniform sensitivity. By using a 5σ detection criterion, we obtained two preliminary lists of sources at $24\ \mu\text{m}$ and $70\ \mu\text{m}$, respectively, constrained by selection criteria similar to those adopted for the catalog of the IRAC sources (see Section 3.3.1).

A comparison between the aperture and PSF photometry methods shows that at $24\ \mu\text{m}$ the aperture photometry tends to systematically overestimate the flux by up to $\sim 50\%$ with respect to the PSF photometry. Similarly, the flux differences at $70\ \mu\text{m}$ are of the same order ($\lesssim 50\%$), but they appear more erratic and without a systematic trend.

In the end, we obtained two more complete lists of sources measured with PSF photometry, containing 1347 and 63 sources at $24\ \mu\text{m}$ and $70\ \mu\text{m}$, respectively, and we used them to supplement the IRAC catalog. Note that among the $24\ \mu\text{m}$ sources we include for completeness six saturated objects, corresponding to InfraRed Source (IRS) 16, 17, 18, 19, 20, and 21 (nomenclature from Liseau et al. 1992). In the MIPS catalog, these correspond to entry IDs = 146, 300, 813, 814, 991, 1018, respectively, that had been flagged with negative $24\ \mu\text{m}$ flux densities, and whose absolute values correspond to the saturation limit (4 Jy).

We adopted angular separation as the criterion for associating the $24\ \mu\text{m}$ and $70\ \mu\text{m}$ sources, requiring that the corresponding centroids be within $20''$; in this way we produced a unique, merged set of sources with MIPS photometry. The merged MIPS catalog is available in the electronic form of this journal (Table 2), and it also contains information on the possible associations of the millimeter sources as reported in previous studies. These associations are based on positional coincidences of the MIPS source centroid being within the beam size of the millimeter observations. A short excerpt from the MIPS catalog is printed in Table 2. The his-

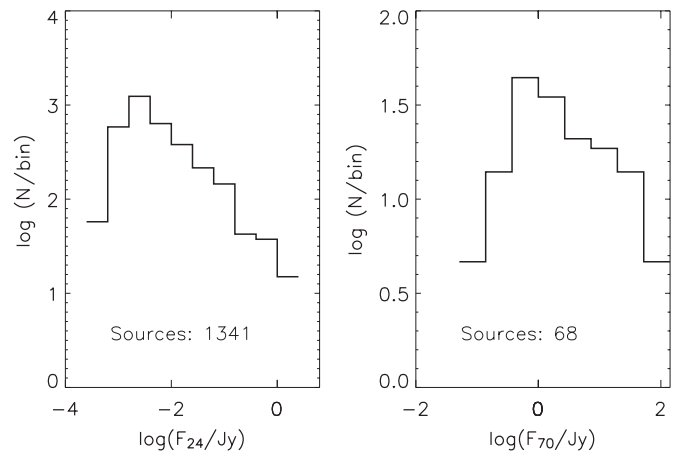


Figure 5. Flux histograms for the VMR-D point sources detected in the MIPS mosaics at $24\ \mu\text{m}$ (left panel) and $70\ \mu\text{m}$ (right panel). In the left panel, six saturated sources corresponding to IRS objects have been discarded (see the text).

togram of the magnitudes is presented in Figure 5, and it shows that the completeness flux densities are essentially the same as those quoted in Giannini et al. (2007), namely, $\approx 2\ \text{mJy}$ at $24\ \mu\text{m}$ and $\approx 300\ \text{mJy}$ at $70\ \mu\text{m}$. Some statistics of the MIPS sources are presented in Table 3.

Given this new MIPS photometry, a re-examination of the color–magnitude diagrams in Giannini et al. (2007, their Figures 7 and 8) is in order. In Figure 6, we present the resulting K versus $K-[24]$ and $[24]$ versus $[24]-[70]$ diagrams, while in Table 4, second and third columns, we report the subdivision in the different classes based on the spectral indexes derived by using the Two Micron All Sky Survey (2MASS) K -band magnitudes as a complement of the present MIPS photometry. This classification scheme is the same used in Giannini et al. (2007) and is based on the correspondence of the color $K-[24]$ with the spectral slope of the different classes adopted by Rebull et al. (2007).

A comparison of the present results with those in Giannini et al. (2007), based on aperture photometry, is possible. We renormalized the values in their Table 5 to reflect the changes in the total number of YSOs; because the measurement of the flux density now has changed by up to 50%, the numbers of sources in each spectral class change as well. We note that

1. the number of MIPS sources detected now in the $24\ \mu\text{m}$ band is increased while at $70\ \mu\text{m}$ it remains practically the same;
2. the percentage of ON-cloud Class I sources is now $\sim 10\%$, which decreased from the previously estimated value of $\sim 30\%$;
3. the percentage of the ON-cloud flat-spectrum sources is approximately the same, $\sim 26\%$, as compared with the previous estimate of $\sim 29\%$; and
4. the percentage of ON-cloud Class II objects is $\sim 62\%$, an increase with respect to the previous estimate of $\sim 37\%$, while Class III sources are now $\sim 2\%$ with respect to the previous value of $\sim 4\%$.

Furthermore, the more accurate modeling of the point sources allows us now to obtain more reliable correspondences between the MIPS, IRAC, and 2MASS objects, alleviating in this way the problem of multiple associations.

In the light of the significantly lower percentage we find here for Class I spectrum sources, we conclude that our previous

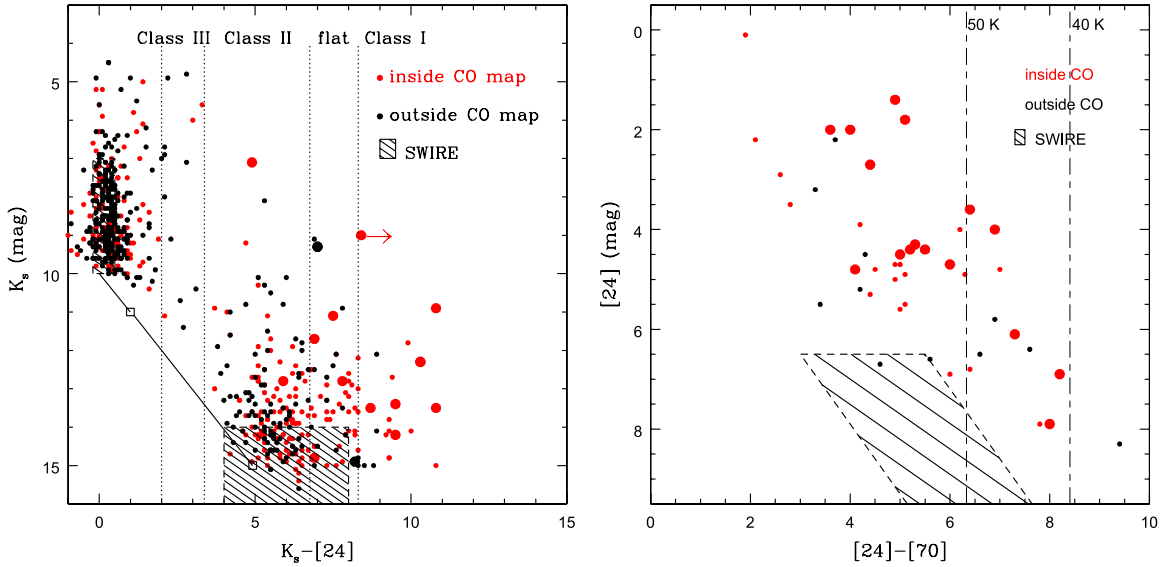


Figure 6. Color–magnitude diagrams for MIPS sources. A comparison with similar diagrams in [Giannini et al. \(2007\)](#) shows that by adopting PSF instead of aperture photometry, a systematic decrease ($\lesssim 50\%$) of the $24\ \mu\text{m}$ flux and random variations (to a lower extent) of the $70\ \mu\text{m}$ one has occurred. As a consequence, the number of Class I sources, estimated through 2MASS and $24\ \mu\text{m}$ photometry (left panel), is now diminished with respect to the early prediction (see also Section 5.2). Moreover, because of the correspondingly larger $[24]-[70]$ color, an increased number of objects now populates the area corresponding to $T < 50\ \text{K}$, in the right panel. (A color version of this figure is available in the online journal.)

Table 2
VMR-D MIPS Catalog: Typical Entries^a

| MIPS ID | R.A.(2000) E70 | Decl.(2000) $\Delta\theta^b$ | Glon IRAC ^c | Glat $^{12}\text{CO}(1-0)^d$ | F24 $^{13}\text{CO}(2-1)^d$ | E24 Dust ^d | F70 |
|---------|------------------------|---------------------------------|---------------------------|---------------------------------|--------------------------------|--------------------------|-----------|
| 1 | 130.79321 0.000e+00 | -44.01385 0.0 | 263.47831 N | -0.97396 N | 8.420e-03 N | 1.812e-03 ... | 0.000e+00 |
| 2 | 130.81630 0.000e+00 | -43.97870 0.0 | 263.46093 N | -0.93919 N | 1.535e-03 N | 1.135e-04 ... | 0.000e+00 |
| ... | ... | ... | ... | ... | ... | ... | ... |
| 135 | 131.38707 0.000e+00 | -43.71376 0.0 | 263.50867 I | -0.45199 N | 4.314e-03 N | 1.037e-04 ... | 0.000e+00 |
| 136 | 131.38847 8.478e-01 | -43.83051 2.1 | 263.60060 I | -0.52397 C | 1.934e+00 C | 2.598e-01 MMS1 | 2.001e+01 |
| ... | ... | ... | ... | ... | ... | ... | ... |

Notes.

^a Coordinates are given in degrees; fluxes (F) and their uncertainties (E) are given in Jy.

^b Angular distance in arcsec between $24\ \mu\text{m}$ and $70\ \mu\text{m}$ centroids.

^c “I” and “N” are used to flag a source as falling inside or outside the IRAC observed region.

^d Symbols are explained in Section 4 (Columns 26–28).

(This table is available in its entirety in a machine-readable form in the online journal. A portion is shown here for guidance regarding its form and content.)

Table 3
MIPS Source Statistics

| CO Association | $24\ \mu\text{m}$ Only | $70\ \mu\text{m}$ Only | 24 and $70\ \mu\text{m}$ | Total |
|----------------------|------------------------|------------------------|----------------------------|-------|
| Inside contours | 604 | 7 | 40 ^a | 651 |
| Outside contours | 131 | 1 | 2 | 134 |
| Outside IRAC catalog | 560 | 8 | 10 ^b | 578 |
| Total | 1295 | 16 ^c | 52 | 1363 |

Notes.

^a Five sources are saturated at $24\ \mu\text{m}$ corresponding to IRS 16, 17, 19, 20, 21; five other sources have a duplicate $70\ \mu\text{m}$ association.

^b One source is saturated at $24\ \mu\text{m}$, corresponding to IRS 18.

^c Four sources are outside the $24\ \mu\text{m}$ mosaic; visual inspection of the remaining shows that nine are diffuse while three appear more compact and are reported in Table 13 as remarkable objects.

Table 4
Classification Based on MIPS and IRAC Photometry

| Class | MIPS Based | | IRAC Based | |
|---------------|----------------------------------|-----------------------------------|---------------------|----------------------|
| | ON-cloud N (%) ^a | OFF-cloud N (%) ^a | ON-cloud N (%) | OFF-cloud N (%) |
| Class I | 16 (10.1) | 4 (3.4) | 44 (9.5) | 5 (2.9) |
| Flat spectrum | 41 (25.9) | 20 (16.9) | 61 (13.2) | 10 (5.7) |
| Class II | 98 (62.0) | 84 (71.2) | 230 (49.7) | 93 (53.4) |
| Class III | 3 (1.9) | 10 (8.5) | 128 (27.6) | 66 (37.9) |

Note. ^a These MIPS-based percentages can be compared with those in Table 5 of [Giannini et al. \(2007\)](#) after renormalization of their values to the YSOs only.

suggestion for an unusual excess of young objects in VMR-D does not hold up based on PSF photometry, and in all future discussions of MIPS sources we shall refer to our current catalog.

4. THE VMR-D POINT-SOURCE CATALOG

Once photometry was obtained, we proceeded to the positional association of the sources detected in the different spectral bands. In this phase of band merging, objects detected at different IRAC wavelengths were considered to be associated if the relative distance of their centroids was less than $1''$. For those cases in which, when comparing two bands, more than one source is found within $1''$, we considered only the nearest source to be associated.

The final VMR-D catalog was produced by including all of the sources detected in *at least* one IRAC band which fulfill all the constraints reported in Section 3.3. An exception to this rule are the 77 sources, mainly corresponding to very bright objects, whose addition we justified in Section 3.3.3. To obtain a coherent list of sources, we restricted the final catalog to the field observed in all four IRAC bands, namely, the region delimited by the yellow contour line in Figure 1.

Obviously, by construction such a catalog contains many sources lacking good photometry in some IRAC bands; only 8796 sources out of the full 170,299 have accurate photometry in all four IRAC bands. However, because for some purposes it is useful to have flux densities in all bands, we choose to give a flux density value in any case. This was done by reconsidering less accurate photometry previously discarded in the source extraction process (see Section 3.3) or, in absence of this photometry, obtaining 5σ upper limits for the source position. Consequently, those missing flux densities in the catalog were recovered from the values that had been previously rejected due to the imposed constraints when the detection falls within a radius of $1''$ from the source position. Note, however, that all these band filling flux densities have been flagged as “bad photometry” in the final lists, in the same way the 5σ upper limits are reported in the catalog for those cases without a specific detection within $1''$. In addition, to allow a more accurate determination of the spectral slopes and a more secure classification of the YSOs, the final catalog also considers the spatial coincidence between the IRAC and MIPS $24\ \mu\text{m}$ sources, and includes the MIPS photometry when the distance between centroids is within $6''$. A larger distance, up to $20''$, has been adopted for MIPS sources detected only at $70\ \mu\text{m}$. These relatively large distances are close to the diffraction radius at $24\ \mu\text{m}$ and $70\ \mu\text{m}$, respectively, and have been adopted to include all the potentially associated sources. Of course, because the probability of the IRAC–MIPS source association decreases with the centroid distance, one must pay increasing attention when the angular distance is larger than $3''$ and $10''$ at $24\ \mu\text{m}$ and $70\ \mu\text{m}$, respectively. Note however that 70% of cases have been found within $3''$. With this criterion, a total of 870 MIPS $24\ \mu\text{m}$ sources have been associated with IRAC sources; out of these, 689 are associated to a single IRAC source, 153 are double associations, 27 are triple, and one is associated with four IRAC sources. To allow the reader to evaluate these associations, we also report in the catalog the distance of the centroids for each association.

The published version of the catalog, available in the electronic form of the journal (Table 5), summarizes the photometry arranging the information it in the following columns:

1. *Column 1.* Source ID. Sources are sorted in ascending order of R.A.
2. *Columns 2 and 3.* Equatorial coordinates (J2000).
3. *Columns 4 and 5.* Galactic coordinates.
4. *Columns 6 and 7.* IRAC flux at $3.6\ \mu\text{m}$ and its uncertainty. When the flux reported is an upper limit, the uncertainty has been put to zero.
5. *Column 8.* Quality flag, assigned as follows: the “good photometry” data are flagged with “H” (High) if they refer to a more than a 10σ detection, and with “L” (Low) if the source is revealed between 5σ and 10σ , respectively; in addition to this, a flag “2” or “1” indicates whether the source lies in the sky area covered in both observing epochs, or only in one of them, respectively. The “bad photometry” data (see above) are flagged with “b,” and upper limits with “u.”
6. *Columns 9–17.* Same as for Columns 6–8, but for the $4.5\ \mu\text{m}$, $5.8\ \mu\text{m}$, and $8.0\ \mu\text{m}$ bands, respectively.
7. *Column 18.* MIPS catalog ID number of the associated MIPS source: this is reported if its centroid is within a distance of $6''$ from the IRAC source. MIPS sources detected only at $70\ \mu\text{m}$ are reported when the centroid is within $20''$. Notice that, due to the different beam sizes, the association of more than one IRAC source with the same MIPS source is allowed.
8. *Column 19.* Distance in arcsec of the associated MIPS source centroid.
9. *Columns 20–22.* MIPS flux density at $24\ \mu\text{m}$, flux uncertainty, and quality flag similar to that used for IRAC flux densities but with good photometry simply flagged “G.” The symbol “NaN” reported for the flux density denotes a position falling outside the MIPS mosaic.
10. *Columns 23–25.* The same as for Columns 20–22 but for the MIPS $70\ \mu\text{m}$ band. Note that for MIPS sources showing only the $70\ \mu\text{m}$ detection (10 cases) the association is reported when the IRAC sources (51 cases) are within $20''$ from the MIPS source.
11. *Columns 26 and 27.* A flag indicating the degree of association with $^{12}\text{CO}(1-0)$ and $^{13}\text{CO}(2-1)$ line emission, respectively, as mapped in Elia et al. (2007). “C” indicates that the IRAC source lies on a map pixel assigned to one or more gas clumps; “A” indicates that the IRAC source is not associated to a clump, but lies inside the integrated intensity contour corresponding to the $5\ \text{K km s}^{-1}$, adopted here as a criterion for spatial association with the gas; “O” indicates a source lying inside the area observed in the given line, but not associated with the gas according to the two previous criteria; and finally, “N” means that the IRAC source is outside the sky area covered by observations in the given line.
12. *Column 28.* Name of the $1.2\ \text{mm}$ dust core, taken from the lists of Massi et al. (2007) and reported here when the IRAC source falls within the quoted core radius.

Examples of the catalog entries are given in Table 5 and some statistics of the catalog content is summarized in Tables 6 and 7.

5. DISCUSSION

YSOs in SF regions can be identified by the presence of an infrared excess which is produced by extended circumstellar disks/envelopes surrounding these objects, and which participates in their pre-main-sequence (PMS) evolution toward the main sequence. For classification purposes, it is customary to

Table 5
VMR-D IRAC Point-Source Catalog: Typical Entries^a

| ID | R.A.(2000) F4.5 E8.0 F70 | Decl.(2000) E4.5 Q8.0 E70 | Glon Q4.5 MIPS ID Q70 | Glat F5.8 $\Delta\theta^b$ $^{12}\text{CO}(1-0)^c$ | F3.6 E5.8 F24 $^{13}\text{CO}(2-1)^c$ | E3.6 Q5.8 E24 Dust ^c | Q3.6 F8.0 Q24 |
|--------|---|--|--------------------------------|---|--|--|-------------------------------|
| 1 | 131.031909 4.15450e-06 0.00000e+00 5.220e-04 | -43.736558 0.00000e+00 u 0.000e+00 | 263.366966 u ... u | -0.667202 2.11600e-05 0.0 N | 1.89903e-05 0.00000e+00 3.084e-04 N | 2.54204e-06 u 0.000e+00 ... | L1 2.87050e-05 u ... |
| ... | ... | ... | ... | ... | ... | ... | ... |
| 393 | 131.096329 8.33412e-03 7.23856e-05 3.907e-04 | -43.775259 2.59158e-04 H1 0.000e+00 | 263.426188 H1 37 u | -0.654711 5.53000e-03 1.7 N | 1.32000e-02 3.59000e-04 2.543e-02 N | 7.87000e-04 b 3.492e-03 ... | b 3.56018e-03 G ... |
| ... | ... | ... | ... | ... | ... | ... | ... |
| 2548 | 131.183726 9.11296e-04 1.79767e-05 1.165e-01 | -43.701613 3.42903e-05 L2 1.191e-02 | 263.407676 H2 57 G | -0.559483 6.48618e-04 5.1 N | 1.42000e-03 5.45410e-05 4.497e-02 N | 8.73000e-05 H1 1.205e-03 ... | b 3.10650e-04 G ... |
| ... | ... | ... | ... | ... | ... | ... | ... |
| 17590 | 131.388578 3.98529e-03 3.38000e-04 8.675e-02 | -43.868336 1.06327e-04 b 0.000e+00 | 263.630227 H2 139 u | -0.547490 3.52000e-03 6.0 C | 2.54057e-03 1.78000e-04 3.754e-01 C | 6.21729e-05 b 4.395e-02 MMS2 | H2 1.29000e-03 G ... |
| ... | ... | ... | ... | ... | ... | ... | ... |
| 170299 | 132.967055 5.54702e-05 0.00000e+00 NaN | -43.592335 6.68016e-06 u 0.000e+00 | 264.135486 H1 ... u | 0.511679 2.14100e-05 0.0 N | 5.86857e-05 0.00000e+00 2.574e-04 N | 5.13993e-06 u 0.000e+00 ... | H1 3.13800e-05 u ... |

Notes.

^a Coordinates are given in degrees; fluxes (F) and their uncertainties (E) are given in Jy; quality flags (Q) are described in Section 4.

^b Angular distance in arcsec between the IRAC and MIPS centroids.

^c Symbols are explained in Section 4, when Columns 26–28 are described.

(This table is available in its entirety in a machine-readable form in the online journal. A portion is shown here for guidance regarding its form and content.)

Table 6
VMR-D Cloud IRAC Catalog Statistics (Global)

| With Good Photometry | Number of Sources |
|-------------------------------------|-------------------|
| In only one IRAC band | 53461 |
| In only two IRAC bands | 97114 |
| In only three IRAC bands | 10851 |
| In all four IRAC bands ^a | 8873 |
| Total number of sources | 170299 |

Note. ^a Including 77 recovered sources with uncertain photometry (see Section 3.3.3).

use the $\log \lambda F_\lambda$ versus $\log \lambda$ plot to derive the spectral slope, α , that is generally evaluated in the $2 \mu\text{m} < \lambda < 20 \mu\text{m}$ range. This parameter is taken to be dependent on the evolutionary phase of the emitting source and its value is generally used to define four classes (Lada 1987; André & Montmerle 1994; Greene et al. 1994): Class I for $\alpha \geq 0.3$, “flat spectrum” for $-0.3 \leq \alpha < 0.3$, Class II for $-1.6 \leq \alpha < -0.3$, and Class III for $\alpha < -1.6$. A further class, Class 0, has been also introduced to include sources that, while escaping any detection at $\lambda < 10 \mu\text{m}$, show relatively strong submillimeter emission (André et al. 1993) and should then correspond to very early and cold objects. This relatively simple classification scheme has been, however, criticized because of its sensitivity to incli-

Table 7
Statistics of Sources Toward VMR-D Cloud (per Band)

| Detections ^a | 3.6 μm | 4.5 μm | 5.8 μm | 8.0 μm |
|--|-------------------|-------------------|-------------------|-------------------|
| S/N ≥ 10 | 100964 | 81945 | 11651 | 6123 |
| And 24 μm | 764 | 801 | 634 | 603 |
| And 24 μm and ^{12}CO | 489 | 504 | 387 | 356 |
| And 24 μm and ^{12}CO and dust | 48 | 50 | 39 | 31 |
| 5 \leq S/N < 10 | 50291 | 48732 | 10442 | 5586 |
| And 24 μm | 96 | 90 | 68 | 43 |
| And 24 μm and ^{12}CO | 59 | 63 | 39 | 22 |
| And 24 μm and ^{12}CO and dust | 3 | 2 | 7 | 3 |
| Bad photometry | 19044 | 39622 | 148206 | 158590 |

Note. ^a Association with a 24 μm source is within 6”, with ^{12}CO is inside the 5 K km s⁻¹ contour level, and with a dust core is considered within the radii quoted in Massi et al. (2007).

nation effects to the line of sight (see, e.g., Robitaille et al. 2007; Crapsi et al. 2008).

Alternative classification schemes based on the bolometric temperature (Myers & Ladd 1993; Chen et al. 1995) or the bolometric luminosity (Young & Evans 2005) have also been proposed in an attempt to minimize the influence of the system inclination to the line of sight. However, these alternative schemes have themselves been found to be sensitive to the system geometry, so that we have decided to adopt the most

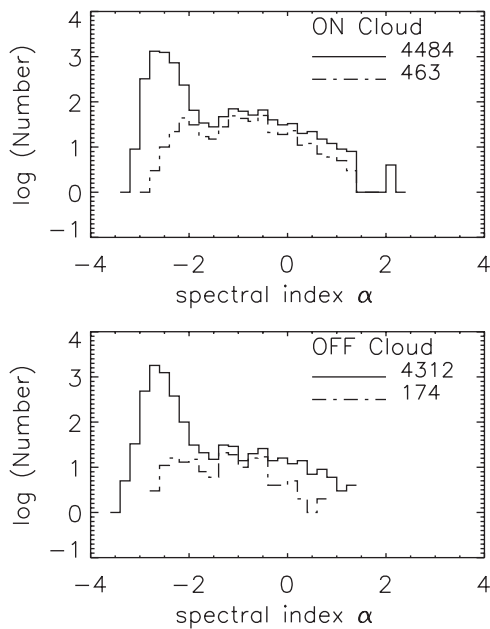


Figure 7. Distribution of the spectral index α , as derived by fitting the source fluxes between 2 and 24 μm (see the text). In both panels, the continuous line refers to the 8796 “working sample” sources (4484 ON-cloud and 4312 OFF-cloud) with good photometry in the four IRAC bands. After subtraction of both normal stars and extragalactic contamination (see the text and Figures 8–10) 637 sources remain, which are located either ON-cloud (dashed line, 463 cases) or OFF-cloud (dashed line, 174 cases).

popular classification scheme based on the spectral slope. This choice also allows us a more direct comparison with a series of studies carried out with *Spitzer* on Galactic star-forming regions in the framework of the legacy project “From Molecular Cores to Planet-forming Disks” (c2d; Evans et al. 2003).

The reader interested in a more detailed discussion on the effects of adopting other classification schemes should refer to Evans et al. (2009, hereinafter E09), who also discussed the role of the extinction corrections.

5.1. Color Analysis and YSO Selection

In the following analysis, we focus our attention on the 8796, out of a total of 170,299, catalog sources for which good photometry was obtained in all the four IRAC bands, i.e., the working sample already defined in Section 1. In addition to this database we also consider, when available, the *K*-band 2MASS photometry and the 24 μm MIPS photometry to allow a more accurate estimate of the spectral index in the 2–24 μm spectral interval.

Our first step was the determination of this spectral index α from the linear fit of the observed $\log \lambda F_\lambda$ versus $\log \lambda$ points for all the working sample sources. The distributions of the α values obtained are shown in the two panels of Figure 7, representing the spectral indexes for ON-cloud (upper) and OFF-cloud (lower) sources, respectively. In the two panels, the histograms are drawn separately for the objects in the working sample (solid line) and for the fraction of the candidate YSOs (dashed line) that have been subsequently selected according to the criteria we shall discuss in the next section.

We note that the number of objects falling within the ON- and OFF-cloud region are quite similar (4484 against 4312). Such a fact derives from the similarity of both areas (0.57 against 0.60 deg^2) and indicates that the overall population of both regions is dominated by photospheres and background/

foreground objects, while the YSO population possibly represents a negligible contribution. This latter is a common feature already found in surveys of other star-forming regions (e.g., Evans et al. 2009; Rebull et al. 2010; Guieu et al. 2009). As a consequence, stringent criteria have to be exploited to select the candidate YSOs.

5.1.1. Source Selection

The ability of the IRAC colors to identify YSOs has been studied by Harvey et al. (2006, 2007) in the Serpens cloud and by Gutermuth et al. (2009) in a large number of YSO clusters, and we use parts of both approaches here, augmented by criteria identifying asymptotic giant branch (AGB) contaminants from Marengo et al. (2008). After considering the locus of the normal reddened stars and the non-negligible extragalactic contamination, these authors suggested two statistical criteria to select candidate YSOs in the [8] versus ([4.5]–[8]) color–magnitude diagram, namely, (1) ([4.5]–[8]) > 0.5 and (2) [8] < 14 – ([4.5]–[8]). This first criterion excludes the stellar component while the second, designed to statistically cut 95% of the extragalactic objects, has been tuned by studying the extragalactic component observed with IRAC in the Elais N1 SWIRE region.

Applying these criteria to the VMR-D cloud, we select 595 ON-cloud and 244 OFF-cloud YSO candidates, respectively. Following Harvey et al. (2006, 2007), to include other potential colder candidates that could have been escaped in this diagram, we also considered further diagrams based on longer wavelength photometry, i.e., the [24] versus ([8.0]–[24]) and [24] versus ([4.5]–[8.0]) diagrams. Adopting the appropriate selection criteria, we included 25 more ON- and 17 OFF-cloud sources. The YSO candidates selected are shown in Figures 8 (ON-cloud) and 9 (OFF-cloud) as open circles and gray crosses, representing objects showing Class I/flat and Class II/III SEDs, respectively.

Also indicated on these plots are the original selection criteria from the Harvey et al. (2006, 2007) studies of the Serpens cloud. However, note that the Serpens cloud (260 pc) is much closer than the VMR-D cloud (700 pc; see Liseau et al. 1992). To reflect this, we have also indicated in the figure the region into which a candidate YSO in Serpens would move if displaced to the VMR-D distance. The region between the two inclined parallel lines can then be regarded as potentially containing both candidate YSOs and extragalactic contaminants meaning that objects in this region should be more accurately studied to ascertain their nature. Here, we conservatively consider only sources delimited by the original criteria represented by the dashed lines in Figures 8 and 9.

In the same figure, the two-color ([3.6]–[4.5]) versus ([5.8]–[8.0]) diagram is also shown in the upper right panel with the same meaning of the symbols, and with a square box that is drawn to show the approximate locus of the Class II sources according to Allen et al. (2004). The irregular area delimited by the dot-dashed line is the locus of the AGB stars in this diagram, according to Marengo et al. (2008). For comparison, in a separate figure (Figure 9), we show the same diagrams drawn for the OFF-cloud sources.

With the aim of obtaining a list of candidate YSOs as clean as possible from contaminants, we also adopted further criteria recently discussed and summarized by Gutermuth et al. (2009). These have been derived for identifying as likely contaminants those sources satisfying a series of constraints, flagging star-forming galaxies and active galactic nuclei (AGNs), as well as shock excited knots that can mimic point sources in

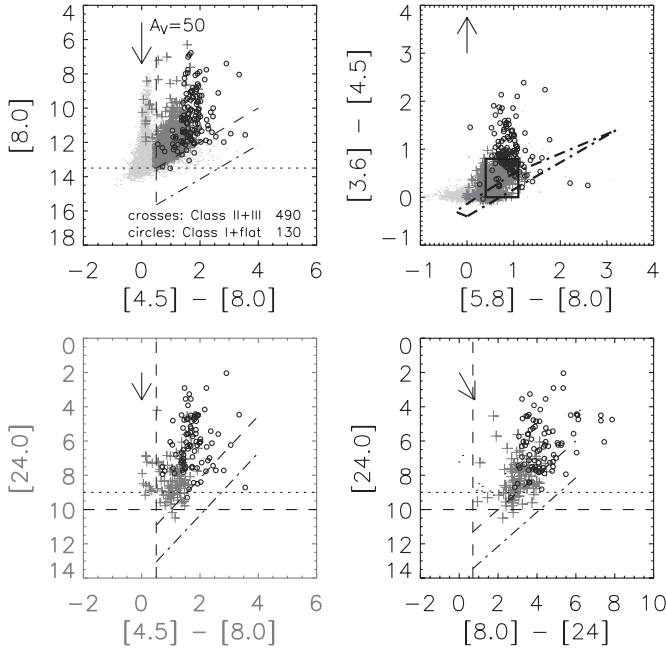


Figure 8. Color–magnitude and color–color diagrams for the VMR-D point sources detected in the four IRAC bands and located ON-cloud (see Section 2). Sources selected applying the Harvey et al. (2006, 2007) criteria are plotted as circles (spectral index $\alpha > -0.3$) and gray crosses ($\alpha < -0.3$). In the upper panels, gray dots represent the 8796 “working sample” sources. The reddening effect, corresponding to a visual extinction of $A_V = 50$ mag, is shown by the arrow (Indebetouw 2005). In the color–magnitude plots the dashed lines correspond to statistical criteria derived by Harvey et al. (2006, 2007) for separating YSO candidates from normal stars (vertical lines) and extragalactic contamination (oblique lines) in the Serpens dark cloud. The dash-dotted line represents the displacement of the dashed line after scaling to the VMR-D distance (see the text). The dotted lines show the completeness limit and the horizontal dashed line shows the $24 \mu\text{m}$ magnitude beyond which a source is considered extragalactic. In the two-color upper right panel, the small square shows the approximate domain for the Class II sources according to Allen et al. (2004). The dot-dashed line encloses the region corresponding to the AGB colors, but note that a source can be considered as a candidate AGB only when two further constraints are satisfied in the $[3.6] - [4.5]$ vs. $[3.6] - [8.0]$ and $[4.5] - [5.8]$ vs. $[5.8] - [8.0]$ diagrams, respectively (Marengo et al. 2008).

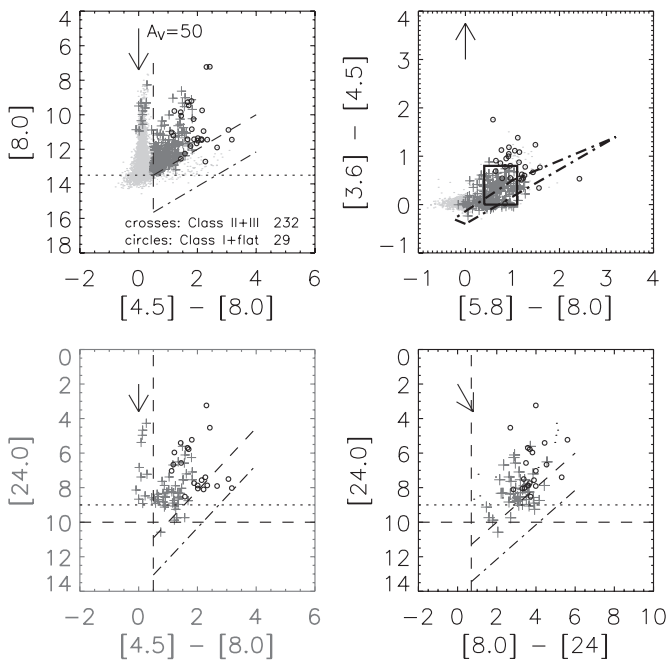


Figure 9. Same as in Figure 8, but for sources located OFF-cloud.

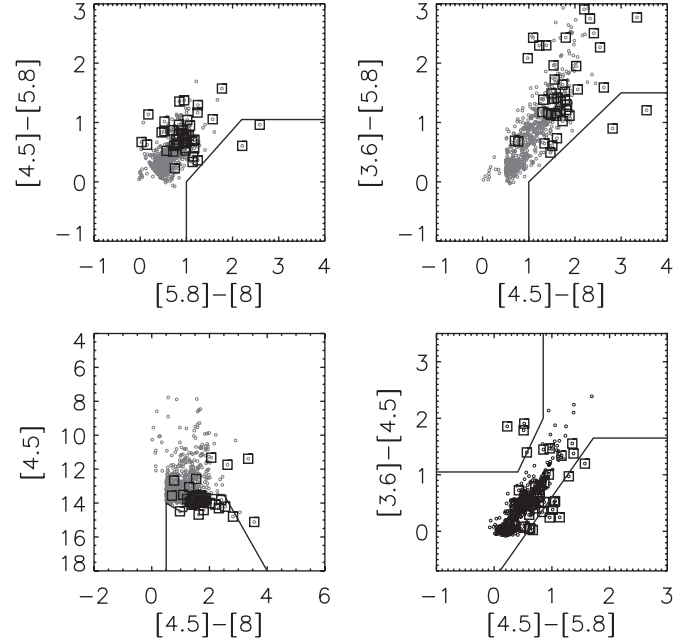


Figure 10. Diagrams used to isolate the contaminants among the sources of the “working sample” selected with the Harvey et al. (2006, 2007) criteria. For simplicity only, ON-cloud sources are displayed. In each diagram, solid lines delimit the loci where possible contaminants are located (see Gutermuth et al. 2009). The gray circles represent the sources shown in Figure 8 as crosses and circles. The upper panels are used to isolate unresolved star-forming galaxies falling under the continuous line. The lower left panel isolates broad-line AGN and the lower right is used to identify likely shock emission (upper left region) and possible cases of polycyclic aromatic hydrocarbon contamination (lower right). Objects falling in at least one of the regions delimited by the continuous lines are identified as likely contaminants and are reported as open squares.

star-forming environments. These are based on color–color diagrams such as $[4.5] - [5.8]$ versus $[5.8] - [8.0]$, $[3.6] - [5.8]$ versus $[4.5] - [8.0]$, and $[3.6] - [4.5]$ versus $[4.5] - [5.8]$, as well as on the color–magnitude $[4.5]$ versus $[4.5] - [8.0]$ diagram.

In Figure 10, we present these diagrams (displaying only the ON-cloud for simplicity) for the sources emerging from the previous selection step that are reported with crosses and circles in Figure 8. Considering the constraints in Gutermuth et al. (2009) we flagged 64 sources, 42 ON- (shown as open squares) and 22 OFF-cloud, which have then been eliminated from our list of candidate YSOs.

As a further check, we also applied to this list the IRAC based criteria of Marengo et al. (2008) for finding AGB contaminants, identifying in this way 115 ON-cloud sources (112 showing a Class III SED) and 65 OFF-cloud (62 showing a Class III SED) sources. These sources have also been eliminated from the final list.

At the end of this process, we remain with 637 IRAC selected candidate YSO sources, 463 ON- and 174 OFF-cloud that we assign to a specific class simply by considering their spectral slope as derived, considering all the available data in the $2 - 24 \mu\text{m}$ spectral interval. These sources have been used to draw the dash-dotted histogram in Figure 7. The corresponding distribution in classes of these candidate YSOs is shown in the fourth and fifth columns of Table 4.

5.1.2. Comparison with Other Star-forming Regions

The analysis presented above allowed us to classify the VMR-D young population and it is interesting to compare our results to those obtained by *Spitzer* for other SF regions. These have been summarized and analyzed in a consistent

Table 8
YSO Classification of the IRAC VMR-D Sources and Comparison with Other Star-forming Regions

| Region | Area (deg ²) | Distance (pc) | YSO Candidate | YSO (deg ⁻²) | YSO (pc ⁻²) | Class I | Flat | Class II | Class III | SFR/Area (M _⊙ Myr ⁻¹ pc ⁻²) |
|------------------------|-----------------------------|------------------|------------------|-----------------------------|----------------------------|------------|------------|-------------|-------------|--|
| ON-cloud ^a | 0.57 | 700 | 620 | 1088 | 7.3 | 60 (9.7%) | 70 (11.3%) | 247 (39.8%) | 243 (39.2%) | 5.5 |
| OFF-cloud ^a | 0.60 | 700 | 261 | 435 | 2.9 | 11 (4.2%) | 18 (6.9%) | 99 (37.9%) | 133 (51.0%) | 2.2 |
| ON-OFF ^b | 0.57 | 700 | 372 | 653 | 4.4 | 50 (13.3%) | 53 (14.2%) | 153 (41.1%) | 117 (31.4%) | 3.3 |
| ON-cloud ^c | 0.57 | 700 | 463 | 812 | 5.4 | 44 (9.5%) | 61 (13.2%) | 230 (49.7%) | 128 (27.6%) | 4.1 |
| OFF-cloud ^c | 0.60 | 700 | 174 | 290 | 1.9 | 5 (2.9%) | 10 (5.7%) | 93 (53.4%) | 66 (37.9%) | 1.5 |
| ON-OFF ^b | 0.57 | 700 | 278 | 522 | 3.5 | 39 (13.2%) | 51 (17.3%) | 142 (47.6%) | 65 (21.9%) | 2.6 |
| ON ^d | 0.57 | 700 | 465 | 816 | 5.5 | ... | ... | ... | ... | 4.1 |
| OFF ^d | 0.60 | 700 | 196 | 326 | 2.2 | ... | ... | ... | ... | 1.6 |
| ON-OFF ^b | 0.57 | 700 | 279 | 490 | 3.3 | ... | ... | ... | ... | 2.5 |
| Cha II | 1.04 | 178 | 26 | 25 | 2.6 | 2 (8%) | 1(4%) | 19 (73%) | 4 (15%) | 0.65 |
| Lupus | 3.10 | 150 | 9 | 30 | 3.3 | 5 (5%) | 10 (11%) | 52 (55%) | 27 (29%) | 0.83 |
| Perseus | 3.86 | 250 | 385 | 100 | 5.2 | 87 (23%) | 42 (11%) | 225 (58%) | 31 (8%) | 1.3 |
| Serpens | 0.85 | 260 | 227 | 267 | 13 | 36 (16%) | 23 (10%) | 140 (62%) | 28 (12%) | 3.2 |
| Ophiucus | 6.60 | 125 | 292 | 44 | 9.3 | 35 (12%) | 47 (16%) | 176 (60%) | 34 (12%) | 2.3 |

Notes.

^a Sources selected with the Harvey et al. (2006, 2007) criteria.

^b Difference counts are weighted by the corresponding solid angles.

^c Contamination subtracted following Gutermuth et al. (2009) and Marengo et al. (2008).

^d Contamination subtracted according to Oliveira et al. (2009).

way by E09 and we adopted it for the VMR-D comparison. However, because our method for selecting the YSOs is not exactly the same as that of E09, before comparing to our results it is desirable to evaluate the effects produced by applying our pipeline to at least one of the five clouds considered by E09. The Serpens cloud is probably the most appropriate for this check: it is projected near the Galactic plane and has been scrutinized with accurate spectroscopic follow-up aimed at identifying AGB contaminants (Oliveira et al. 2009). For this cloud, we did not attempt to select candidate YSOs out of the full catalog, delivered by the c2d legacy project, and made available at the *Spitzer* Science Center, because our selection criteria are similar to those used to obtain the c2d YSO list. The difference in our approach is mainly in the identification of the contaminants, so we used the Serpens YSO catalog to analyze the 262 sources listed with our procedure. Applying our pipeline, based on the Gutermuth et al. (2009) criteria, from this list we exclude a total of 14 sources. None of these are in the list of the 78 candidate YSOs scrutinized by Oliveira et al. (2009) and their distribution in classes is two sources in Class I, two are flat-spectrum, eight in Class II, and two in Class III. Despite our exclusion of these 14 sources out of the 262 in the Serpens YSO catalog, we note that after their subtraction from the numbers quoted in E09 and reported in Table 8, the relative distribution in classes remains practically the same and the SF rate is also not significantly affected. In the limit of this indication, we can compare in Table 8 the results obtained for VMR-D with those provided by E09, noting that in the numbers quoted for the YSOs in Serpens the sources identified as AGB by Oliveira et al. (2009) have been already subtracted.

In this table, rows 1–3 consider the sources selected by means of the Harvey et al. (2007) criteria and shown in Figures 8 and 9. The subsequent rows, 4–6, report the results obtained after filtering the sources in the first three rows with more stringent criteria for eliminating extragalactic and galactic contaminants (Gutermuth et al. 2009; Marengo et al. 2008) as illustrated in Figure 10. The further three rows, namely, 7–9, are used to present the results obtained after applying to the first three rows

the correction for contaminants suggested by Oliveira et al. (2009) on the basis of their spectroscopic investigations of the Serpens YSO population selected with the Harvey et al. (2007) criteria.

Indeed, because Serpens is an SF region quite close to the Galactic plane ($l \sim 5^\circ$), it is reasonable to assume that its level of contamination of AGB and giant stars is comparable to that of VMR-D. The sample of YSOs in Serpens is contaminated by background giants to a level of about 25% so that, by applying the same correction to our VMR-D ON- and OFF-cloud sample, we obtain the statistics given in Table 8, lines 7–9. Note that in this case we do not report the class distributions because the 25% contamination is with respect to the total number of YSOs.

In lines 10–14, we also report for comparison the values of the corresponding quantities quoted by E09 for Cha II, Lupus, Perseus, Serpens, and Ophiucus. In each line, we give the investigated area, the adopted cloud distance, the total number of YSOs found, the surface density per solid angle and per square parsec, the number of objects of type Class I, flat-spectrum, Class II, and Class III, respectively, and finally the derived SF rate.

First of all, we recall that, as opposed to these other SF regions, VMR-D is located in the Galactic plane and it is also from two to five times farther away. As already mentioned, the latter circumstance imposes a larger value for the limiting luminosity (typically $0.1 L_\odot$ instead of, e.g., $0.004 L_\odot$ for the Taurus) resulting in significant contamination from stars; conversely, it offers the opportunity to study the SF process where the mass reservoir is the largest available.

As a rough first approximation, we consider the OFF-cloud statistics as representative of the average population of the Galactic plane and, as such, it could be subtracted from the ON-cloud statistics after weighting for the different areas, in this way estimating the uncontaminated young population of VMR-D. By doing this, we obtain lines 3, 6, and 9, of Table 8, with the caution that the OFF-cloud region could be active in SF as suggested by the histograms in Figure 7, albeit at a lower level. Because of this and of the larger luminosity limit, the numbers

Table 9
VMR-D IRAC Candidate YSO List: Typical Entries^a

| IRAC ID | R.A.(2000) | Decl.(2000) | Glon | Glat | F3.6 | E3.6 | Q3.6 |
|---------|-------------|-------------|------------|----------------|-----------------------|-----------------------|-------------|
| | F4.5 | E4.5 | Q4.5 | F5.8 | E5.8 | Q5.8 | F8.0 |
| | E8.0 | Q8.0 | MIPS ID | $\Delta\theta$ | F24 | E24 | Q24 |
| | F70 | E70 | Q70 | α^b | ¹² CO(1–0) | ¹³ CO(2–1) | Dust |
| 4378 | 131.224365 | −43.926624 | 263.602173 | −0.676375 | 1.02738E-03 | 2.88283E-05 | H1 |
| | 9.57767E-04 | 3.59507E-05 | H1 | 1.23024E-03 | 3.53127E-05 | H1 | 1.36355E-03 |
| | 4.95515E-05 | H1 | ... | 0.0 | 2.721E-04 | 0.000E+00 | u |
| | 1.199E-03 | 0.000E+00 | u | −0.60 | N | N | ... |
| ... | ... | ... | ... | ... | ... | ... | ... |
| 38674 | 131.603989 | −43.704887 | 263.599640 | −0.323964 | 2.85320E-03 | 7.00859E-05 | H2 |
| | 3.52582E-03 | 6.94163E-05 | H2 | 4.25391E-03 | 8.60992E-05 | H2 | 5.84348E-03 |
| | 9.94560E-05 | H2 | 261 | 1.1 | 4.539E-02 | 8.235E-04 | G |
| | 9.515E-04 | 0.000E+00 | u | 0.53 | C | N | umms1 |
| ... | ... | ... | ... | ... | ... | ... | ... |

Notes.

^a Symbols and units as in Table 5, unless otherwise specified. Sources selected out of the working sample.

^b Spectral index of the source.

(This table is available in its entirety in a machine-readable form in the online journal. A portion is shown here for guidance regarding its form and content.)

reported here for the YSOs should actually be considered lower limits. However, taken at face value, they suggest an excess of Class III (~22%) and a deficit of Class II objects (~48%) with respect to the other SF regions. The cause of the apparent excess of Class III objects might be either evolution—the Vela cloud is older than these others—or due to uncorrected contamination of AGB stars (see E09).

Considering the statistics corrected for extragalactic and galactic contaminants, reported in the fourth and sixth lines, makes the class distributions of the YSOs in VMR-D resemble more those seen in Serpens and Ophiuchus rather than in other SF regions. Differences actually exist in the Class II/III relative ratios, but they probably stem from an incomplete correction since VMR-D is more embedded in the plane than Serpens is. If we try to account for such discrepancies, we can reasonably rule out evolutionary effects since the relatively large fraction of Class III sources in VMR-D does not reflect a particularly small fraction of Class I and flat-spectrum sources that instead appear relatively numerous. Moreover, if we calculate the SF rate per square parsec, by assuming a mean mass of $1 M_{\odot}$, a binary fraction of 0.5, and a period of 2 Myr for SF (E09), we obtain for the VMR-D the SF rate $\approx 2.5\text{--}4.1 M_{\odot} \text{ Myr}^{-1} \text{ pc}^{-2}$, a range of values which is more consistent with that of the younger clouds like Serpens, Ophiucus, and Perseus, than it is for the smaller corresponding values obtained for Lupus and Chamaleon.

It is also noteworthy that adopting the corrections suggested by Oliveira et al. (2009) we obtain (Table 8, lines 6–8) very similar results to those obtained after considering the set of criteria discussed in Section 5.1.1 to exclude likely contaminants (lines 4–6). This adds some confidence to the present results.

Given these observational indications, it seems plausible to consider the VMR-D age as being in the range 1–2 Myr, in good agreement with the dynamical time estimate of 1.5 Myr derived by Elia et al. (2007) for VMR-D and comparable to the estimates for Perseus (Palla & Stahler 2000) and Serpens (Djupvik et al. 2006). Within the previous assumptions, and given the solid angle subtended by our ON-cloud region, it is easy to estimate that approximately $200\text{--}300 M_{\odot} \text{ Myr}^{-1}$ are converted into stars in the investigated region. Because the cloud mass has been estimated at $1.5 \times 10^4 M_{\odot}$ (Elia et al. 2007), we can also derive the depletion time for the cloud,

which is $t_{\text{depl}} \approx 40\text{--}70$ Myr, as well as the SF efficiency given by $M_{\text{YSO}}/(M_{\text{YSO}} + M_{\text{cloud}}) \approx 0.02\text{--}0.03$. However, the uncertainty associated with the estimate of the cloud mass is at least $\Delta M/M \sim 50\%$ so that these quantities are correspondingly uncertain.

5.2. IRAC versus MIPS-based Classification and Final Lists of YSO

We have seen that the IRAC data are an essential, additional ingredient of YSO classification, and by including them we have been able to reconcile (as indeed was anticipated by Giannini et al. 2007) the estimated excess of Class I objects previously derived using only MIPS aperture photometry.

In this section, we want to briefly discuss the young population census, as obtained by means of the present IRAC photometry complemented with 2MASS and MIPS data, with the results that can be derived using only 2MASS and MIPS photometry. The aim is to assess the ability of the MIPS photometry to correctly classify YSOs when no IRAC data are available, as is the case for the MIPS regions without overlap with the IRAC mosaics (see Figure 1).

The classification method used in these two cases is different: in the first case the 2MASS/IRAC/MIPS photometric data are used to evaluate the spectral slope α and to separate candidate YSOs from contaminants, while in the second case only 2MASS/MIPS data are used to exploit the K_s versus $K_s\text{--}[24]$ diagram as in Giannini et al. (2007). The first method is clearly the most appropriate, involving more photometric information (up to six wavelengths); however, being the second method, the alternative choice when MIPS observations are the only available, it is interesting to check if differences arise in selecting the YSO population with these two methods. The two lists of candidate YSOs obtained with these two approaches are reported in the corresponding catalogs in the electronic journal (Tables 9 and 10). Typical entries for both are reported in Tables 9 and 10, respectively.

In discussing the differences emerging between these two approaches, we shall limit ourselves to consider only the corresponding lists of Class I objects; similar comparisons for the other classes (flat, II, or III) follow the same line of thinking.

Table 10
VMR-D MIPS Candidate YSO List: Typical Entries^a

| MIPS ID | R.A.(2000) E70 | Decl.(2000) $\Delta\theta$ | Glon K_s-24^b | Glat IRAC ID | F24 $^{12}\text{CO}(1-0)$ | E24 $^{13}\text{CO}(2-1)$ | F70 Dust |
|---------|------------------------|-------------------------------|--------------------|-------------------|------------------------------|------------------------------|---------------------|
| 37 | 131.09596 0.000E+00 | -43.77494 0.0 | 263.42578 4.70 | -0.65472 393 | 2.543E-02 N | 3.492E-03 N | 0.000E+00 ... |
| ... | ... | ... | ... | ... | ... | ... | ... |
| 546 | 131.92834 3.890E-02 | -43.73021 1.2 | 263.76633 10.30 | -0.15719 74548 | 1.163E+00 C | 8.047E-02 O | 3.519E+00 umms11 |
| ... | ... | ... | ... | ... | ... | ... | ... |

Notes.

^a Symbols and units as in Table 2, unless otherwise specified.

^b K_s-24 color index in magnitudes.

(This table is available in its entirety in a machine-readable form in the online journal. A portion is shown here for guidance regarding its form and content.)

Before proceeding, we reiterate that the census of the different classes in this paper is based on the working sample, i.e., is limited to those sources with valid fluxes in all four IRAC bands. This clearly excludes the sources with an upper limit, a large flux uncertainty, or even a not strictly point-like shape in at least one IRAC band. These objects, although not considered here, are included in the general catalog and could represent interesting targets for future investigations.

The 49 sources selected as Class I objects by scrutinizing the IRAC catalog working sample are listed in Table 11. Along with the source ID, coordinates, and spectral index, we also report the presence of a counterpart in other bands: $K_s-2\text{MASS}$ in Column 5 and MIPS bands in Columns 6–8. This information is needed to compare the two methods since the MIPS classification is based on $K_s-2\text{MASS}$ and $24\ \mu\text{m}$ magnitudes, and only IRAC sources associated with both these ancillary data are subject to both IRAC and MIPS classification. By looking at Table 11 (Column 9), we see that only five sources out of the 49 entries were classified with MIPS and all of these are Class I (flag “I”). While this is the expected result when the four IRAC points are reasonably well aligned with the two extreme spectral points at K_s and $24\ \mu\text{m}$, it is however noteworthy that in the relatively few cases in which both methods can be applied they give the same classification. In Columns 10 and 11, we also indicate whether the source is associated with gas and dust emission. In this respect, the genuine nature of the selected Class I sources is attested to by the fact that 44 out of the 49 sources are coincident with gas clumps or peaks. The remaining five sources are located in regions not covered by the ^{12}CO map (flag “N”). Finally, the last column indicates whether we find that the source is also IRAC variable on a timescale of 4.5 months (Giannini et al. 2009); we identify six cases of variability.

Table 12 is complementary to Table 11. It provides the list of all 20 sources classified as Class I based on $K_s-2\text{MASS}$ and $24\ \mu\text{m}$ photometry. Besides the K_s-24 index (Column 4), information is also given about the presence of a $70\ \mu\text{m}$ counterpart (Column 5). The association with an IRAC counterpart is indicated in Column 6 while Column 7 reports the quality flags of the detections in the four IRAC bands. Since this classification is determined by MIPS, there are only seven sources (see Column 8) contained in the IRAC working sample, while 11 further sources are associated with IRAC objects lacking good photometry in one or more bands. The remaining two sources do not have a counterpart in the IRAC catalog (see the notes to Table 12).

Five objects in this table are clearly in common with Table 12 but there are two more cases included in the working sample and classified as flat-spectrum sources when we derive the spectral slope exploiting the IRAC data. This suggests that the classification independently provided by $K_s-2\text{MASS}/\text{MIPS}$ and $K_s-2\text{MASS}/\text{IRAC}/\text{MIPS}$ is not completely equivalent even if the two methods seem to be in agreement in five out of the seven common cases encountered. Again, most of these sources are located in gas clumps. Note also that Table 12 contains many sources whose IRAC flags do not fulfill our compelling requirements (only H1 and H2 quality flags). Although they are not members of the working sample, they are nonetheless good candidates for very young protostars.

Finally, for the sake of completeness, we present in Table 13 a list of MIPS-selected sources that, for various reasons, can be considered as particularly red or cold. When observed in both MIPS bands, these objects have a color $[24]-[70] > 6.3$, a condition we imposed to select the coldest ($T < 50\ \text{K}$) sources (see Figure 6, right panel). Other sources listed in Table 13 are (1) the $70\ \mu\text{m}$ sources with point-like appearance but without a $24\ \mu\text{m}$ counterpart and (2) the objects saturated at $24\ \mu\text{m}$, but already classified as IRAS Class I objects (Liseau et al. 1992). Note that increasing the angular distance of the association, reported in Column 7, also increases the uncertainty so that further analysis is required to confirm a genuine source association.

5.3. Clustering

The spatial distribution of the young stars provides useful information about SF mechanisms in the cloud, since YSOs do not move very far from their birthplaces during the PMS evolution. Much of the accumulated observational evidence suggests that stars prefer to form in groups, and in particular, that the two-point correlation function of young stars shows a different behavior at small and large spatial scales, respectively (see, e.g., Simon 1997). More recently, Gutermuth et al. (2009) analyzed the spatial distribution of the YSOs in 36 clusters by means of both the nearest neighbor and the minimum spanning tree method. A critical length, in the range $\sim 0.1-0.5\ \text{pc}$, could be identified in the cumulative distribution of the source spacings indicating differences in the slope at small and large spatial scales. We use here the function $w(\theta)$ to quantify the degree of the YSOs clustering in the VMR-D cloud:

$$w(\theta) = \frac{N_p(\theta)}{N_0(\theta)} - 1, \quad (1)$$

Table 11
Class I YSOs Selected with 2MASS/IRAC/MIPS Data

| IRAC ID ^b | $\alpha(2000)$ (deg) | $\delta(2000)$ (deg) | α | K_s 2MASS | MIPS ID | Q24 | Q70 | MIPS Class ^c | ¹² CO (1–0) | Dust Core ^a | IRAC Variable ^d |
|----------------------|----------------------|----------------------|----------|-------------|---------|-----|-----|-------------------------|------------------------|------------------------|----------------------------|
| 17793 | 131.390823 | −43.872124 | 0.61 | Y | ... | u | u | ... | C | MMS2 | N |
| 18177 | 131.395065 | −43.882664 | 0.37 | Y | ... | u | u | ... | C | ... | Y |
| 18652 | 131.400284 | −43.891411 | 0.82 | N | ... | u | u | ... | C | ... | N |
| 19225 | 131.406204 | −43.917553 | 1.16 | N | ... | u | u | ... | C | ... | N |
| 19354 | 131.407394 | −43.918594 | 0.66 | Y | ... | b | u | ... | C | ... | N |
| 21173 | 131.426315 | −43.456017 | 0.62 | N | ... | u | u | ... | N | ... | N |
| 21825 | 131.432907 | −43.451939 | 0.59 | N | 166 | G | G | ... | N | ... | N |
| 22179 | 131.436584 | −43.448711 | 0.61 | Y | ... | u | u | ... | N | ... | N |
| 22262 | 131.437500 | −43.447865 | 0.31 | Y | ... | u | u | ... | N | ... | N |
| 23011 | 131.445084 | −43.389664 | 1.29 | N | 172 | G | G | ... | N | ... | N |
| 38674 | 131.603989 | −43.704887 | 0.53 | Y | 261 | G | u | I | C | umms1 | N |
| 39589 | 131.613586 | −43.711151 | 1.25 | N | 270 | G | G | ... | C | umms1 | N |
| 41404 | 131.632233 | −43.910416 | 1.39 | N | ... | u | u | ... | C | MMS4 | N |
| 41429 | 131.632477 | −43.549744 | 1.04 | N | 290 | G | u | ... | C | ... | N |
| 41786 | 131.636246 | −43.911308 | 0.89 | Y | ... | u | u | ... | C | MMS4 | N |
| 44510 | 131.664520 | −43.380684 | 0.55 | N | 316 | G | u | ... | C | ... | Y |
| 47368 | 131.694290 | −43.336273 | 0.54 | Y | ... | u | u | ... | C | ... | N |
| 47436 | 131.694946 | −43.887310 | 1.37 | N | 347 | G | u | ... | C | ... | N |
| 48046 | 131.701172 | −43.886124 | 1.08 | N | 352 | G | u | ... | C | MMS5 | N |
| 50748 | 131.727905 | −43.876759 | 0.67 | Y | 386 | G | u | I | C | ... | Y |
| 55956 | 131.776840 | −43.322323 | 0.50 | N | 426 | G | u | ... | C | ... | N |
| 65153 | 131.855423 | −43.815571 | 1.03 | N | 473 | G | G | ... | C | ... | N |
| 65198 | 131.855774 | −43.814709 | 0.73 | Y | 473 | G | G | ... | C | ... | N |
| 67878 | 131.877563 | −43.472893 | 0.30 | N | 497 | G | u | ... | C | ... | Y |
| 67896 | 131.877747 | −43.467525 | 0.33 | N | 498 | G | u | ... | C | ... | N |
| 68154 | 131.880020 | −43.898384 | 1.10 | N | 503 | G | G | ... | C | ... | N |
| 68231 | 131.880646 | −43.896694 | 0.43 | N | 503 | G | G | ... | C | ... | N |
| 70412 | 131.897675 | −43.356682 | 0.45 | N | 521 | G | u | ... | C | ... | N |
| 72549 | 131.913589 | −43.438141 | 0.54 | N | ... | u | u | ... | C | ... | N |
| 84160 | 131.999054 | −43.653702 | 0.43 | N | 601 | G | u | ... | C | ... | N |
| 101621 | 132.129349 | −43.517223 | 0.85 | N | 717 | G | u | ... | C | ... | N |
| 102538 | 132.136902 | −43.515751 | 0.79 | N | ... | u | u | ... | C | ... | N |
| 104823 | 132.155701 | −43.281319 | 0.51 | N | 746 | G | u | ... | C | umms22 | N |
| 104849 | 132.155991 | −43.280067 | 0.36 | N | 746 | G | u | ... | C | umms22 | N |
| 106972 | 132.173294 | −43.529209 | 1.78 | N | 775 | G | G | ... | C | MMS9 | N |
| 108306 | 132.184921 | −43.268906 | 1.44 | N | 787 | G | G | ... | C | ... | N |
| 111144 | 132.209610 | −43.519905 | 1.83 | N | 825 | G | u | ... | C | MMS14 | N |
| 112469 | 132.221695 | −43.515335 | 2.11 | N | 838 | G | G | ... | C | MMS16 | N |
| 112472 | 132.221710 | −43.636738 | 0.94 | Y | 840 | G | u | I | C | ... | N |
| 113053 | 132.227066 | −43.553127 | 0.59 | Y | ... | u | u | ... | C | ... | N |
| 114979 | 132.244598 | −43.639202 | 2.02 | N | 858 | G | G | ... | C | MMS17 | N |
| 120812 | 132.302841 | −43.633789 | 0.54 | Y | ... | b | u | ... | C | ... | N |
| 120962 | 132.304306 | −43.596691 | 0.73 | Y | ... | u | u | ... | C | MMS20 | Y |
| 122296 | 132.318268 | −43.612213 | 0.35 | N | 947 | G | u | ... | C | MMS21 | N |
| 124358 | 132.339371 | −44.030910 | 0.73 | N | ... | u | u | ... | C | ... | N |
| 124521 | 132.340988 | −44.033684 | 2.07 | N | ... | u | u | ... | C | ... | Y |
| 137019 | 132.466995 | −43.378731 | 0.46 | Y | 1108 | G | u | I | C | ... | N |
| 138002 | 132.477051 | −43.388687 | 0.87 | Y | 1120 | G | u | I | C | ... | N |
| 139510 | 132.491974 | −43.381367 | 0.88 | N | 1130 | G | u | ... | C | umms26 | N |

Notes.^a Dust core names are from Massi et al. (2007).^b Sources selected out of the working sample.^c Classification based on the diagram K_s versus $K_s-[24]$ (see Figure 6).^d IRAC variability on a timescale of 6 months (Giannini et al. 2009).

where $N_p(\theta)$ is the average number of pairs with angular separation between θ and $\theta + \Delta\theta$ around each object, and $N_0(\theta)$ is the same number expected for a random distribution of the same sources. For SF regions, this function for PMS objects typically shows a power-law behavior $w(\theta) \propto \theta^{-\gamma}$, but with clearly different exponents for small ($\gamma \approx 2$) and large ($\gamma \approx 0.5$) spatial

scales, respectively (e.g., Leinert et al. 1993; Larson 1995; Simon 1997). This fact has been interpreted as an indication of a critical scale that separates the regime of binary and multiple stars, at smaller scales, from the hierarchical clustering dominating at larger scales. Larson (1995) also suggested that this scale could represent the Jeans length of the molecular

Table 12
Class I YSOs Selected with 2MASS/MIPS Data

| MIPS ID | $\alpha(2000)$ (deg) | $\delta(2000)$ (deg) | K_s-24 (mag) | F70 | IRAC Counterpart | IRAC Flags | IRAC Class ^a | ¹² CO (1–0) | Dust Core |
|------------------|----------------------|----------------------|----------------|-----|------------------|-------------|-------------------------|------------------------|-----------|
| 93 | 131.29494 | -43.75684 | 8.50 | N | 8642 | H1 H2 H1 H2 | f | N | ... |
| 130 | 131.38113 | -43.89581 | 8.90 | N | 16862 | b H2 b u | ... | N | ... |
| 138 | 131.38982 | -43.87410 | 9.90 | N | 17713 | b H2 H2 H2 | ... | C | MMS2 |
| 261 | 131.60376 | -43.70510 | 9.30 | N | 38674 | H2 H2 H2 H2 | I | C | umms1 |
| 308 | 131.65639 | -43.87086 | 10.80 | Y | 43665 | H2 b b b | ... | C | ... |
| 315 ^b | 131.66409 | -43.88627 | 8.70 | Y | ... | ... | ... | C | ... |
| 386 | 131.72771 | -43.87690 | 10.80 | N | 50748 | H2 H2 H2 H2 | I | C | ... |
| 541 | 131.91966 | -43.43661 | 9.20 | N | 73282 | b H2 b H2 | ... | C | umms10 |
| 546 | 131.92834 | -43.73021 | 10.30 | Y | 74548 | H2 H2 H2 b | ... | C | umms11 |
| 576 | 131.96498 | -43.42231 | 9.50 | Y | 79572 | H2 H2 H2 b | ... | C | ... |
| 729 | 132.14119 | -43.51330 | 9.50 | Y | 103109 | H2 H2 b H2 | ... | C | ... |
| 814 | 132.20293 | -43.54186 | 8.40 | Y | 110380 | b b b b | ... | C | MMS12 |
| 840 | 132.22160 | -43.63700 | 9.30 | N | 112472 | H2 H2 H2 H2 | I | C | ... |
| 884 ^c | 132.26060 | -44.40168 | 8.80 | N | ... | ... | ... | N | ... |
| 921 | 132.29868 | -43.59826 | 9.40 | N | 120425 | H2 H2 H2 H2 | f | C | MMS20 |
| 928 | 132.30367 | -43.60686 | 10.80 | Y | 120963 | b b H2 H2 | ... | C | MMS21 |
| 1108 | 132.46693 | -43.37880 | 9.30 | N | 137019 | H2 H2 H2 H2 | I | C | ... |
| 1114 | 132.47073 | -43.68967 | 8.90 | N | 137393 | b H2 H2 H2 | ... | O | ... |
| 1120 | 132.47690 | -43.38887 | 9.30 | N | 138002 | H2 H2 H2 H2 | I | C | ... |
| 1170 | 132.54562 | -43.28630 | 10.00 | N | 144801 | H1 H2 H1 b | ... | C | MMS29 |

Notes.^a Classification based on the spectral index.^b Embedded in very bright nebulosity near IRS 17.^c Observed at 24 μ m only.

Table 13
Other Remarkable Objects Selected with MIPS

| MIPS ID ^a | $\alpha(2000)$ (deg) | $\delta(2000)$ (deg) | F24 | F70 | IRAC Counterpart | IRAC Flags | Distance (arcsec) | ¹² CO (1–0) | Dust Core |
|----------------------|----------------------|----------------------|-----|-----|------------------|-------------|-------------------|------------------------|-----------|
| 31 | 131.03918 | -44.00486 | N | Y | ... | | | N | ... |
| 48 | 131.13193 | -43.83388 | Y | Y | ... | | 3.4 | N | ... |
| 146 ^b | 131.39792 | -43.85200 | S | Y | 18476 | b b b b | 2.8 | C | ... |
| 288 | 131.63107 | -43.92499 | Y | Y | 41283 | b b b b | 0.5 | C | MMS4 |
| 294 | 131.63802 | -43.92678 | Y | Y | 41975 | b b b b | 0.9 | C | MMS4 |
| 300 ^b | 131.64540 | -43.91031 | S | Y | ... | | 6.5 | C | MMS4 |
| 315 | 131.66409 | -43.88627 | Y | Y | ... | | 16.0 | C | ... |
| 642 | 132.04202 | -43.35051 | Y | Y | 90122 | H2 H2 L2 L2 | 0.8 | C | ... |
| 657 | 132.06612 | -43.78766 | Y | Y | 93485 | b H2 b u | 2.2 | C | umms16 |
| 661 ^c | 132.06978 | -43.78875 | Y | Y | 93906 | H2 H2 H2 H2 | 0.9 | C | umms16 |
| 813 ^b | 132.20084 | -42.90561 | S | Y | ... | | 4.9 | N | ... |
| 814 ^b | 132.20293 | -43.54186 | S | Y | 110380 | b b b b | 2.1 | C | MMS12 |
| 917 | 132.29530 | -43.49447 | Y | Y | 120052 | H2 H2 u u | 3.2 | O | ... |
| 923 | 132.30054 | -44.27600 | Y | Y | ... | | 11.1 | O | ... |
| 925 ^d | 132.30151 | -43.27896 | N | Y | 120280 | H2 H2 u u | 14.6 | C | ... |
| 951 | 132.32057 | -43.93255 | Y | Y | 122524 | u b u L2 | 0.1 | C | ... |
| 991 ^b | 132.35916 | -43.28617 | S | Y | 126339 | b b b b | 1.5 | C | MMS22 |
| 998 | 132.36937 | -44.07478 | Y | Y | 127325 | b b b b | 1.5 | C | MMS23 |
| 1018 ^b | 132.38667 | -44.18056 | S | Y | ... | | 3.6 | C | MMS26 |
| 1247 ^e | 132.65999 | -43.82816 | N | Y | 156273 | u b H2 H2 | 12.0 | N | ... |
| 1306 | 132.87169 | -43.52266 | Y | Y | ... | | 9.3 | N | ... |

Notes.^a All the sources fall in the area mapped with IRAC and MIPS (24 μ m and 70 μ m).^b Sources saturated at 24 μ m: nos. 146, 300, 813, 814, 991, and 1018 corresponding to IRS 16, 17, 18, 19, 20, and 21 of Liseau et al. (1992), respectively.^c Classified as Class II with IRAC.^d Barely visible at 70 μ m, in the other bands this position corresponds to the boundary of a spherical blob (2' in diameter); the IRAC source could not be a genuine association due to the large distance (Column 8).^e Barely visible at 70 μ m; at 24 μ m there is a very strong diffuse emission and a faint object is visible at a distance of $\sim 12''$ NW. This faint source is excluded from the 24 μ m list because of the constraints imposed to the PSF-fitting parameters (see Section 3.5).

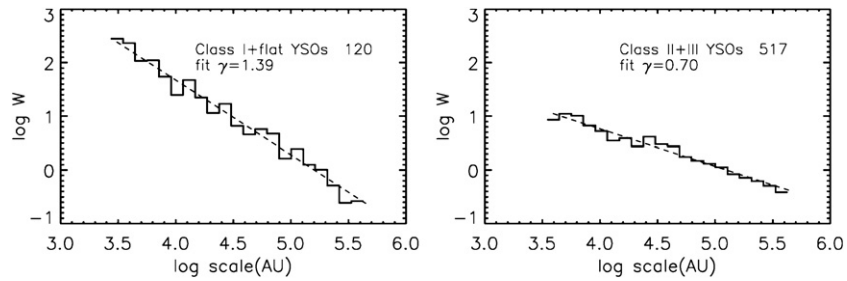


Figure 11. Two-point correlation function for all the candidate YSOs in VMR-D cloud. Left panel: sources classified as Class I and flat-spectrum. Right panel: Class II and III sources. The number of objects is reported in each panel with the slope γ of the linear fit. The slope uncertainty, evaluated by bootstrap resampling, is ± 0.10 and ± 0.08 in the left and right panels, respectively.

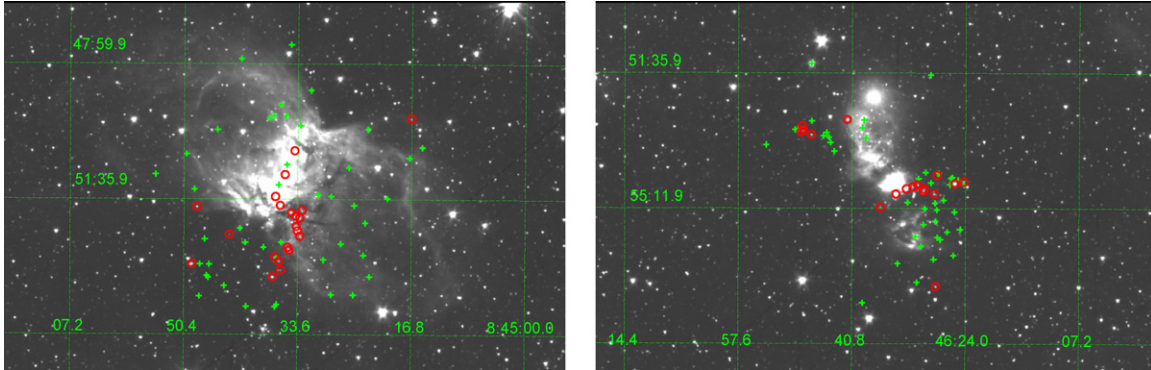


Figure 12. Class I and flat-spectrum (red circles) and Class II and III (green crosses) IRAC sources found in a radius of $4'$ around IRS 16 (left panel) and IRS 17 (right panel), respectively. Sources shown here possess at least three IRAC flux densities of good quality (see the text). (A color version of this figure is available in the online journal.)

cloud, although this interpretation encounters difficulties in explaining the different length scales observed in the Taurus, Ophiuchus, and Trapezium clusters (Simon 1997).

We applied the $w(\theta)$ statistics to our candidate YSOs selected among the VMR-D working sample sources (see Section 5.1), that is, those sources satisfying the criteria for minimizing the presence of galactic and extragalactic contaminants illustrated in Section 5.1.1 and Figures 8–10. The spatial distribution of these sources is presented in Figure 2 where the objects of Class I/flat (red circles) and Class II/III (green crosses) are shown superposed on the $8.0 \mu\text{m}$ IRAC mosaic.

We find substantial differences between clustering in early and late classes as shown in Figure 11, where we present the behavior of the $w(\theta)$ function for Class I and flat-spectrum (left panel), and Class II and III sources (right panel), respectively. It is apparent that in both cases the correlation function behaves as a single power law, at least in the investigated range of scales, but with noticeably different slopes denoting a higher degree of clustering of the younger classes with respect to the later evolutionary stages. This can be also qualitatively seen by eye from the spatial distributions in Figure 2.

Note, however, that in the range of the investigated spatial scales, there is no break in the power-law slope within each region; this is significant even though a direct comparison with the cases discussed in Simon (1997) for optically selected PMS stars is not straightforward because here we deal with IRAC selected YSOs instead of optically selected PMS stars. A more appropriate comparison can be done with Harvey et al. (2007) who show the behavior of the same $w(\theta)$ function computed for the distribution of the YSOs in Serpens (their Figure 10). The slopes they found for both Class I/flat and Class II/III sources are remarkably similar to those shown in Figure 11 for VMR-D

sources. A possible difference may be due to a trend in Serpens toward smaller scales due to a flattening of the function at scales smaller than $\approx 5 \times 10^3$ AU.

A plausible justification for the different slopes of early and late YSOs is simply that it is due to the different ages of the two populations. It is generally accepted that stars are essentially formed in clusters, so that it is naturally expected that the older objects have moved from their birthplaces, producing the object dispersal that we measure in the shallower slope of the correlation function for Class II/III sources.

Finally, in Figures 12 and 13, we show more details of the four regions around IRS 16, 17, 19, and 20, including the spatial distributions of the Class I/flat (red circles) and Class II/III (green crosses) located within $4'$. To produce these figures, we consider an enlarged sample containing all the catalog sources located around the IRS objects and with good photometry in at least two adjacent IRAC bands. This allows us to compensate for the relative scarcity in these small areas of candidate YSOs selected from our working sample and then to better highlight the trend in the spatial distribution of the different classes. The sources reported here have been selected from this enlarged sample by applying the same criteria discussed in Section 5.1.1 and illustrated in Figures 8–10. In doing this, we discarded the sources with upper limits and considered only those cases for which at least a bad photometry was obtained in the two complementary IRAC bands.

In all cases, we see that around these four IRS objects the Class I/flat sources (red circles) are not uniformly distributed. They appear more abundant around IRS 16 and IRS 17; Class II/III objects (green crosses) are instead more numerous and more symmetrically distributed in IRS 16, 19, and 20. An exception is IRS 17 where the Class II/III objects follow the

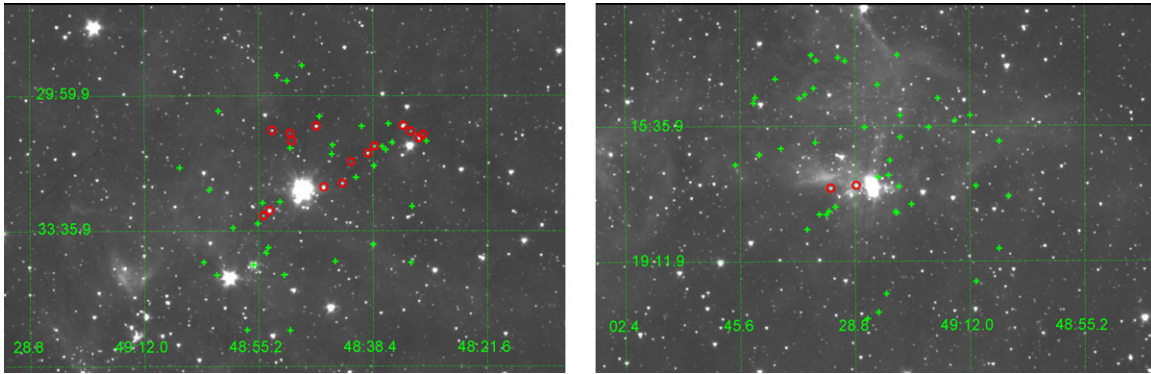


Figure 13. Same as in Figure 12, but for the regions around IRS 19 (left panel) and IRS 20 (right panel), respectively. (A color version of this figure is available in the online journal.)

same elongated distribution of the Class I/flat sources. We also note that this configuration in IRS 17 is suggestive of the presence of two separated clusters as has also been suggested by Massi et al. (2006). Speculating on this case, we suggest that a dust disk, whose plane is perpendicular to the observed YSO distribution, may be responsible for this appearance; this is also suggested by the central dark lane visible in all the IRAC bands. It is however clear that a conclusion cannot be given here and further investigations are needed.

6. CONCLUSIONS

This paper presents the analysis of the *Spitzer*-IRAC mosaics obtained in the region of VMR, Cloud D. In an ≈ 1.2 deg² area, corresponding to the overlap of the IRAC mosaics in the four bands, we obtained the photometry that has been used to compile a four-band point-source catalog. This has been supplemented by relevant information at longer wavelengths from revised photometry of the VMR-D MIPS mosaics and from previously published millimeter line and continuum observations of the same region. This catalog has been used to outline the general characteristics of the YSOs in this SF region. The main results are as follows.

1. The VMR-D IRAC point-source catalog has been compiled with 170,299 entries, 8796 of which constitute our working sample, and have good quality fluxes in all four IRAC bands. Complementary information has been also added using revised, PSF-based, MIPS 24 μ m and 70 μ m photometry and previous millimeter observations obtained in both CO lines and dust continuum.
2. A revised catalog containing the point sources extracted from the VMR-D MIPS 24 μ m and 70 μ m mosaics has also been obtained following the same photometric procedure adopted for the IRAC bands.
3. The working sample has been analyzed according to the spectral slope that was obtained by also considering both the K_s -2MASS and the MIPS 24 μ m fluxes when available.
4. We selected the candidate YSOs by means of their position in color-color and color-magnitude diagrams involving IRAC and MIPS photometry; the likely contaminants due to extragalactic and galactic objects have also been estimated and excluded from the final list of YSOs constituted by 637 objects.
5. The candidate YSOs have been used to evaluate the surface density (3.3–5.5 pc⁻²), the SF rate (2.5–4.1 M_{\odot} Myr⁻¹ pc⁻²) and efficiency (≈ 0.02 –0.03), and the depletion time (40–70 Myr) of the VMR-D cloud.

6. The global clustering properties of the YSOs, studied by means of the two-point correlation function, have been found to be very similar to those derived by Harvey et al. (2007) for the Serpens SF region; it clearly shows that Class I/flat sources are more clustered than Class II/III sources.
7. The IRAC catalog sources around IRS 16 and IRS 17 show a larger fraction of Class I/flat SEDs with respect to IRS 19 and IRS 20 where the Class II/III objects are relatively more numerous. In the IRS 17 region, there is a tendency for the Class II/III to trace the same elongated distribution of the Class I/flat sources.

We thank Joao Lin Yun, Luca Olmi, and Berlinda Maiolo for many helpful discussions. D.E. has been partly supported by the European Commission FP6 Marie Curie Research Training Network CONSTELLATION (MRTN-CT-2006-035890). F.S. acknowledges partial support by the Italian Space Agency (ASI). This work is based on observations made with the *Spitzer Space Telescope*, which is operated by the Jet Propulsion Laboratory, California Institute of Technology under a contract with NASA. Support for this work was provided by NASA through an award issued by JPL/Caltech.

REFERENCES

- Allen, L. E., et al. 2004, *ApJS*, 154, 363
 André, P., & Montmerle, T. 1994, *ApJ*, 420, 837
 André, P., Ward-Thompson, D., & Barsony, M. 1993, *ApJ*, 406, 122
 Chen, H., Myers, P. C., Ladd, E. F., & Wood, D. O. S. 1995, *ApJ*, 445, 377
 Crapsi, A., van Dishoeck, E. F., Hogerheijde, M. R., Pontoppidan, K. M., & Dullemond, C. P. 2008, *A&A*, 486, 245
 De Luca, M., Giannini, T., Lorenzetti, D., Massi, F., Elia, D., & Nisini, B. 2007, *A&A*, 474, 863
 Djupvik, A. A., et al. 2006, *A&A*, 458, 789
 Elia, D., et al. 2007, *ApJ*, 655, 316
 Evans, N. J., II., et al. 2003, *PASP*, 115, 965
 Evans, N. J., II., et al. 2009, *ApJS*, 181, 321 (E09)
 Fazio, G. G., et al. 2004, *ApJS*, 154, 10
 Giannini, T., et al. 2005, *A&A*, 433, 941
 Giannini, T., et al. 2007, *ApJ*, 671, 470
 Giannini, T., et al. 2009, *ApJ*, 704, 606
 Greene, T. P., Wilking, B. A., Andre, P., Young, E. T., & Lada, C. J. 1994, *ApJ*, 434, 614
 Guieu, S., et al. 2009, *ApJ*, 697, 787
 Gutermuth, R. A., Megeath, S. T., Myers, P. C., Allen, L. E., Pipher, J. L., & Fazio, G. G. 2009, *ApJ*, 184, 18
 Harvey, P. M., et al. 2006, *ApJ*, 644, 307
 Harvey, P. M., et al. 2007, *ApJ*, 663, 1149
 Indebetouw, R., et al. 2005, *ApJ*, 619, 931
 Lada, C. J. 1987, in IAU Symp. 115, Star Forming Regions, ed. M. Peimbert & J. Jugaku (Dordrecht: Reidel), 1

- Larson, R. B. 1995, *MNRAS*, [272](#), [213](#)
- Leinert, Ch., et al. 1993, *A&A*, [278](#), [129](#)
- Liseau, R., Lorenzetti, D., Nisini, B., Spinoglio, L., & Moneti, A. 1992, *A&A*, [265](#), [577](#)
- Lorenzetti, D., Giannini, T., Vitali, F., Massi, F., & Nisini, B. 2002, *ApJ*, [564](#), [839](#)
- Marengo, M., Reiter, M., & Fazio, G. G. 2008, in *AIP Conf. Proc.* 1001, IXth Torino Workshop on Evolution and Nucleosynthesis in AGB stars and the 2nd Perugia Workshop on Nuclear Astrophysics, ed. R. Guandalini, S. Palmerini, & M. Busso (Melville, NY: AIP), [331](#)
- Massi, F., De Luca, M., Elia, D., Giannini, T., Lorenzetti, D., & Nisini, B. 2007, *A&A*, [466](#), [1013](#)
- Massi, F., Lorenzetti, D., & Giannini, T. 2003, *A&A*, [399](#), [147](#)
- Massi, F., Lorenzetti, D., Giannini, T., & Vitali, F. 2000, *A&A*, [353](#), [598](#)
- Massi, F., Testi, L., & Vanzì, L. 2006, *A&A*, [448](#), [1007](#)
- Murphy, D. C., & May, G. 1991, *A&A*, [247](#), [202](#)
- Myers, P. C., & Ladd, E. F. 1993, *ApJ*, [413](#), [L47](#)
- Oliveira, I., et al. 2009, *ApJ*, [691](#), [672](#)
- Palla, F., & Stahler, S. W. 2000, *ApJ*, [540](#), [255](#)
- Rebull, L. M., et al. 2007, *ApJS*, [171](#), [447](#)
- Rebull, L. M., et al. 2010, *ApJS*, [186](#), [259](#)
- Robitaille, T. P., Whitney, B. A., Indebetouw, R., & Wood, K. 2007, *ApJS*, [169](#), [328](#)
- Schuster, M. T., Marengo, M., & Patten, B. M. 2006, *Proc. SPIE*, [6270](#), [65](#)
- Simon, M. 1997, *ApJ*, [482](#), [L81](#)
- Stetson, P. B. 1987, *PASP*, [99](#), [191](#)
- Werner, M. W., et al. 2004, *ApJS*, [154](#), [1](#)
- Wouterloot, J. G. A., & Brand, J. 1999, *A&AS*, [140](#), [177](#)
- Yamaguchi, N., Mizuno, N., Saito, H., Matsunaga, K., Mizuno, A., Ogawa, H., & Fukui, Y. 1999, *PASJ*, [51](#), [775](#)
- Young, C. H., & Evans, N. J., II. 2005, *ApJ*, [627](#), [293](#)